Chapter 6.

Structural, morphological and rheological properties of WSe_2 with emphasis on radiation induced phenomena

6.1 Introduction

This chapter shifts focus to tungsten diselenide (WSe_2), another transition metal dichalcogenide (TMDC) system that shares many isotropic characteristics with the WS_2 system. While WS_2 has been extensively studied in the earlier chapters, this chapter highlights the distinctive characteristics and potential of WSe_2 material. Although both materials possess similar layered structures, the key distinction lies in the substitution of selenium atoms in WSe_2 for the sulfur atoms in WS_2. This change in chalcogen element, along with differences in atomic size and electronegativity, significantly influences their physical and electronic properties, making them well-suited for a range of emerging applications [1]. Following the widespread exploration of WS_2, the WSe_2 system has also garnered comparable scientific interest, particularly in understanding its structure-property relationships. Unlike most TMDCs, which typically exhibit *n*-type semiconducting behaviour, WSe_2 is a *p*-type semiconductor [2]. This *p*-type nature of current conduction, along with enhanced stability and resistance to oxidation, helps facilitate semi-metallic characteristics. Consequently, WSe_2 has exhibited significant benefits in possible device deployment [3–5].

Ionizing radiation, charged particle beams, and swift heavy energetic ions are often considered to modify and manifest the physical properties of materials [6]. Among these techniques, ion irradiation offers better controllability and spatial precision in tailoring the defect type and concentration, making it a more suitable method for controlled defect generation. Recent efforts have focused on improving device fabrication by incorporating doping and defect patterning at the atomic level of the system to reveal novel physical phenomena. It can lead to isolated defects, clusters of point defects, columnar defects, defect annealing, and defect segregation in the material exposed to the radiation, depending on the mass and energy of the ions [7]. As a result, irradiation has emerged as an effective technique for defect engineering in a wide range of 2D materials. It is well established that defects in a semiconducting material can largely influence and modify the device performances. There are ample reports on the generation of novel structures and device performances through defect formation, phase transitions, structural transformations, doping via ion irradiation, etc., in 2D materials [8, 9].

Understanding the effects of ionizing and ion beam irradiation on WSe_2 is essential for determining the applicability of WSe_2-based electronic devices in extreme radiation environments. For instance, in space applications, materials must withstand cosmic rays,

which are primarily composed of heavy charged particles and protons, posing a significant challenge to device stability over a prolonged duration of time [10]. Nevertheless, strong evidence of exceptional optical stability in WSe_2 monolayers, even after continuous γ-radiation exposure, was reported by Elafandi *et al*. [11]. Stanford *et al.* reported selective introduction of defects in few-layer WSe_2 by tuning the material's transport properties and resistivity through controlled irradiation dose using a focused He^+ ion beam [12].

Based on these instances, this chapter explores the effects of γ-irradiation on WSe_2, using doses ranging from 10 kGy to 40 kGy. The irradiated WSe_2 nanosystems were subsequently dispersed in a NaCMC polymer selected as a host matrix to examine the rheological behaviour of the WSe_2/NaCMC nanocomposites. Moreover, the effects of low-energy 15 keV helium (He^{2+}) and 15 keV carbon (C^{2+}) ion irradiation on WSe_2 are investigated. The chapter also examines the modifications in the structural, vibrational and morphological properties of layered WSe_2 with 60 MeV nitrogen (N^{5+}) ions, supported by first-principles calculations to explore the effect of clusters of defects on the electronic band structure.

6.2 WSe_2 nanosystems under γ-ray exposure and irradiation with 15 keV He^{2+}, 15 keV C^{2+} and 60 MeV N^{5+} ions

For the γ-irradiation study, exfoliated WSe_2 samples were prepared using a co-solvent strategy involving isopropyl alcohol (IPA) and water to effectively separate layers from the bulk WSe_2 material. The exfoliated WSe_2 samples were then placed in a γ-irradiation chamber at UGC-DAE CSR, Kolkata, where they were exposed to γ-rays using a ^{60}Co source similar to the WS_2 case. The irradiation doses marked were 0 kGy (un-irradiated), 10 kGy, 25 kGy, 30 kGy, 35 kGy, and 40 kGy. After receiving the designated γ-dose, the samples were removed from the chamber and utilized for further analysis.

Furthermore, WSe_2 systems were irradiated using low-energy 15 keV He^{2+} and C^{2+} ions. These experiments were conducted at the Variable Energy Cyclotron Centre (VECC) in Kolkata, utilising the K130 variable energy cyclotron equipped with a 6.4 GHz electron cyclotron resonance (ECR) ion source. Bulk WSe_2 systems were irradiated with He^{2+} ions, whereas C^{2+} irradiation was performed on exfoliated forms of the materials synthesized through liquid phase exfoliation (LPE) using 1-methyl-2-pyrrolidone (NMP) as a solvent. For the irradiation experiments, the samples were prepared in powdered form and

compressed into pellets using a 1.3×1.3 cm^2 area round teflon base. These pellets were then mounted on a flat rectangular ladder to ensure proper alignment for the ion beam. The experiments were conducted inside a high-vacuum target chamber at a ~10^{-6} mbar pressure. For He^{2+} irradiation at low energy of 15 keV, bulk WSe_2 systems were irradiated at fluences of 1×10^{15} ions/cm^2, 5×10^{15} ions/cm^2 and 1×10^{16} ions/cm^2 under a normal incidence (0°). Additionally, at a particular fluence of 5×10^{15} ions/cm^2, bulk WSe_2 systems were irradiated at an oblique angle of 55°. Similarly, WSe_2 systems in exfoliated form were irradiated with 15 keV C^{2+} ions at fluences of 1×10^{15} ions/cm^2, 3.5×10^{15} ions/cm^2, 7.5×10^{15} ions/cm^2, and 1×10^{16} ions/cm^2 under normal incidence. The beam current was monitored and maintained using a Faraday cup integrated into the chamber. An operating voltage of 7.5 kV and a maximum current of 1.5 μA were applied to achieve the +2 charge state for the projectile ions.

For the 60 MeV N^{5+} ion irradiation experiment, exfoliated WSe_2 powder synthesized via a liquid-phase exfoliation (LPE) using NMP as the solvent and was subjected to swift heavy ion (SHI) exposure using the 15 UD Pelletron tandem accelerator at the Inter-University Accelerator Centre (IUAC) in New Delhi, India. The exfoliated WSe_2 powder was pressed into pellets with a teflon base, which were then mounted on a four-faced rectangular ladder and placed inside a high-vacuum target chamber (pressure ~5×10^{-6} mbar). Before irradiation, the ion beam was scanned over a quartz reference to ensure a uniform, collimated and stable beam over a size of 1×1 cm^2. Subsequently, teflon-supported few-layer WSe_2 samples were irradiated at normal incidence with ion fluences of 5×10^{11} ions/cm^2, 1×10^{12} ions/cm^2, 1×10^{13} ions/cm^2, and 5×10^{13} ions/cm^2. Throughout the procedure, the beam current, typically of around 1 pnA, was regularly monitored to maintain a stable and consistent beam on the samples.

6.3 Structural, vibrational and rheological study of γ-irradiated WSe_2 systems

6.3.1 Structural and vibrational analysis

The powder XRD patterns of both un-irradiated and γ-irradiated WSe_2 samples, exposed to radiation doses ranging from 10 kGy to 40 kGy are represented in Fig. 6.1 (a). Distinct diffraction peaks are observed at ~13.75°, 41.86°, and 56.84°, corresponding to the (002), (006), and (008) crystallographic planes, respectively, indexed with the help of JCPDS card no. 38-1388 [13]. These patterns confirm the hexagonal crystal structure of the WSe_2 system, which belongs to the space group *P63/mmc* (No. 194). The most prominent peak

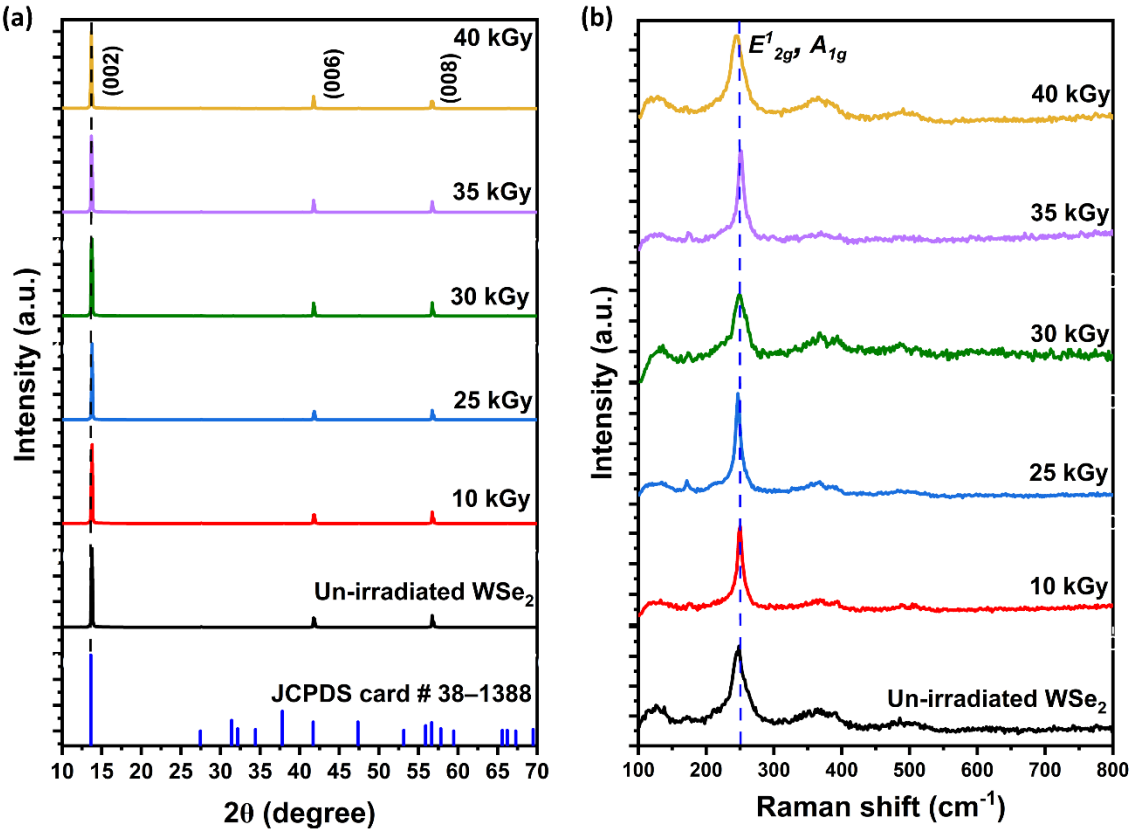

Figure 6.1: (a) Powder XRD patterns, (b) Raman spectra of un-irradiated and irradiated WSe_2 exposed to 10-40 kGy doses of γ-rays.

at ~13.75°, associated with the (002) plane, is consistent across all samples, indicating a favoured orientation along the *c*-axis direction. The lattice parameters were determined by fitting the most intense (002) peak using the Voigt function, revealing a variation from ~12.89 Å to 12.95 Å with increasing γ-dose. A shifting of the (002) peak toward lower 2θ values suggests lattice expansion, i.e., an increase in the interlayer spacing after γ-irradiation. This expansion is likely due to the creation of a localized strain or the formation of vacancies, most likely sulfur vacancies induced by γ-ray exposure.

The Raman spectra of both un-irradiated and γ-irradiated WSe_2 samples, exposed to doses ranging from 10 to 40 kGy are shown in Fig. 6.1 (b). The prominent first-order Raman modes, namely the in-plane E^1_{2g} and out-of-plane A_{1g} modes, originate from vibrations involving W-Se and Se-Se atomic bonds in the WSe_2 system. These modes are characterized by a distinct sharp peak merged near ~249 cm^{-1}, having almost the same frequency [14]. Moreover, several multi-phonon scattering peaks appear, particularly involving the longitudinal acoustic (*LA*) mode, which arises owing to the second-order

Raman processes. These second-order modes arise from the coupling of phonon modes of nonzero momentum, where the electronic transitions are associated with excitonic states [15]. One such combined mode, A_{1g}-LA, appears as a broadened peak at around 128 cm^{-1} in the low-wavenumber region. In the high-wavenumber region, another Raman peak appears at ~363 cm^{-1}, attributed to the E^1_{2g}+LA mode. Furthermore, a defect-related peak emerges at ~172 cm^{-1}, identified as the $LA(M)$ mode.

6.3.2 Rheological response of the WSe_2/NaCMC polymeric solution

The rheological analysis was carried out from the flow curves to gain an insight into the shear flow behaviour of prepared WSe_2/NaCMC nanocomposite solutions. This study was carried out by dispersing WSe_2 nanosheets in NaCMC polymer solution before and after irradiation at 10 kGy and 35 kGy of γ-dose. The flow behaviour was acquired at a constant temperature of 25 °C in a shear rate range of 1-1000 s^{-1} to determine the fluid consistency and dynamic viscosity represented in Fig. 6.2. The WS_2/NaCMC nanofluids illustrate a non-Newtonian fluid with shear-thinning behaviour (Fig. 6.2 (a)). This is a characteristic of a pseudoplastic behaviour. The complex interaction between the fluid and the nano filler essentially governs the non-Newtonian behaviour [16]. The shear-thinning characteristic may be attributed to the constant shearing of NaCMC-based WSe_2 nanocomposites in an aqueous suspension, which can align with the direction of flow. A decrease in viscosity with increasing shear rate can be seen from Fig. 6.2 (b). To be mentioned, a slight drop in the viscosity curve was observed in the 10 kGy irradiated WSe_2/NaCMC nanocomposite solutions, and then it got increased at 35 kGy as compared to the un-irradiated system. Irradiation can facilitate the separation of van der Waals-bonded WSe_2 layers, allowing them to slide more easily over each other within the polymeric matrix due to their lubricating properties [17]. However, at a higher dose of 35 kGy, agglomeration of WSe_2 may occur, leading to an increase in viscosity as discussed in the case of the γ-irradiated WS_2 system in Chapter 3.

Moreover, the flow curves for each sample were fitted with the Herschel-Bulkley model, which is a modified version of the power law model. It consists of three or more parameters to define the complex relation between shear stress and shear rate of fluids represented by [18],

$$\tau = \tau_0 + K.\dot{\gamma}^m, \tag{6.1}$$

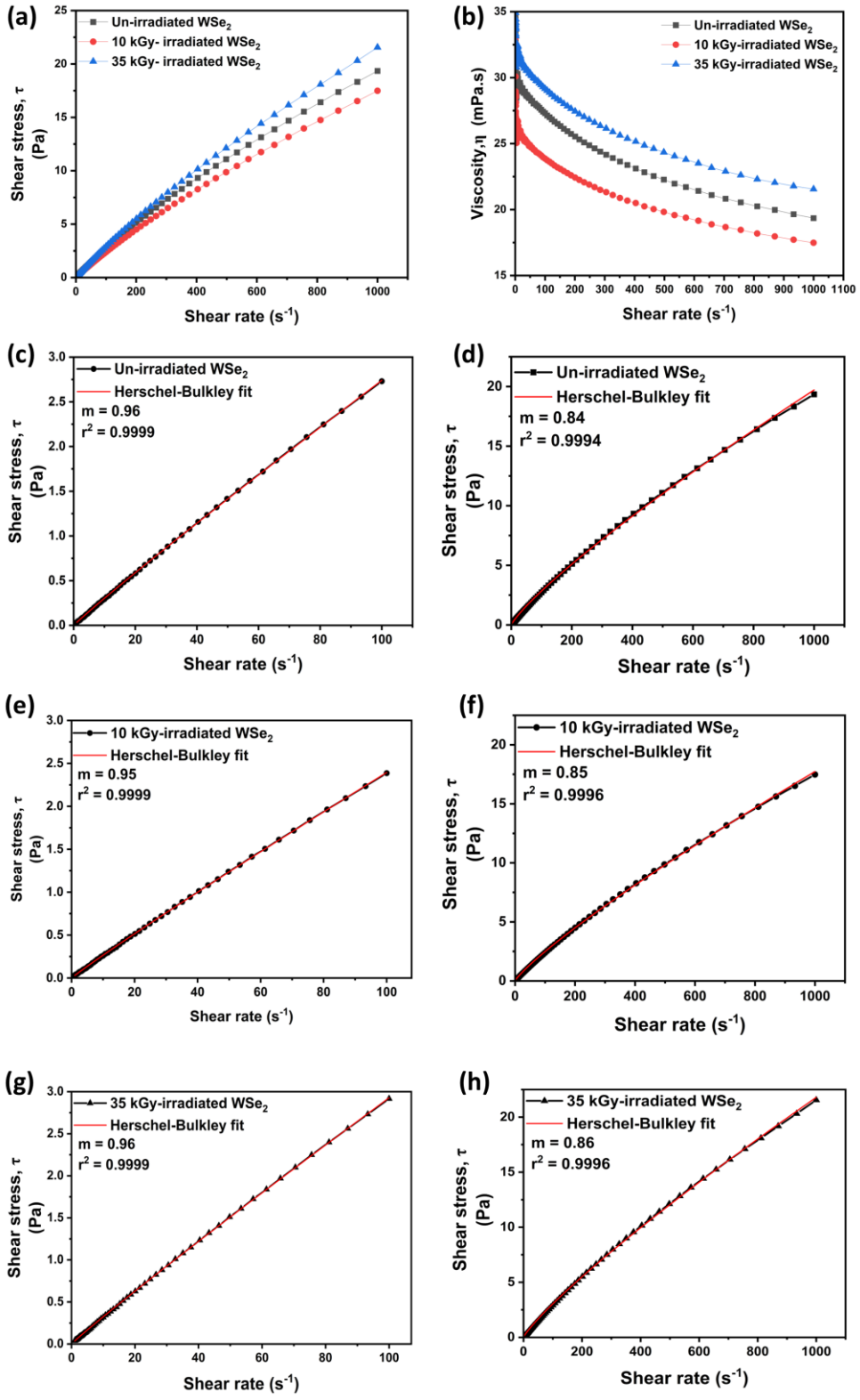

Figure 6.2: (a) Shear stress, (b) viscosity curves, and Herschel-Bulkley fitted plots of shear stress *vs*. shear rate curves of (c,d) un-irradiated WSe_2 and γ-irradiated WSe_2 at (e,f)10 kGy and (g,h) 35 kGy in the range of 0-100 s^{-1} and 0-1000 s^{-1}, respectively, with zero yield stress as a function of shear rate.

where τ is the shear stress, τ_0 is the yield stress, m is the power index, $\dot{\gamma}$ is the shear rate, and K is a consistency index. So, when τ_0 has a non-zero value and $m = 1$, it represents the Bingham model, whereas when τ_0 is close to 0 in the Herschel-Bulkley model, it becomes equivalent to the power-law model,

$$\tau = K.\dot{\gamma}^m \tag{6.2}$$

Through these fitted plots shown in Fig. 6.2 (c-h), the fluid behaviour index (m) is estimated in the low shear rate range of 100 s^{-1} and the moderate shear rate range of 1000 s^{-1}, which specifies the nature of the fluid. In all cases, the m values were found to be slightly below 1, i.e. 0.95-0.96, at the lower shear rate, indicating near-Newtonian behaviour. However, as the shear rate increases to 1000 s^{-1}, the m values decline to the range of ~0.84-0.86, signifying a transition from Newtonian to non-Newtonian (shear-thinning) behaviour of nanofluids. The consistency index, K, estimated in the moderate shear rate range of 1000 s^{-1}, was roughly ~0.06 for both un-irradiated WSe_2 and the sample irradiated at 35 kGy of γ-dose, dispersed in NaCMC solution. While the 10 kGy γ-irradiated WSe_2/NaCMC nanocomposite solution exhibited a slightly lower K value of around 0.05, which displayed lower viscosity. Besides, bar graphs are plotted by calculating the power law index m through fitted plots across different shear rate ranges to illustrate the transition from Newtonian behaviour (m close to 1) to non-Newtonian behaviour ($m < 1$) as the shear rate increases from low to moderate amounts, as shown in the *Appendix* (Fig. A11).

Furthermore, the temperature-dependent viscosity measurements were performed in the range of 5-80 °C at a constant shear rate (50 s^{-1} with pre-shear for 180 s), with a temperature ramp of 2 °C/min shown in Fig. 6.3(a). From the plot, the dynamic viscosity is adequately decreased in all the cases with increasing temperature till 80 °C. A hump observed at a critical temperature around 55-65 °C suggests structural modifications within the WSe_2/NaCMC polymeric solutions. This feature may also be associated with the glass transition temperature of the NaCMC polymer [19, 20]. Furthermore, the bar plot shown in Fig. 6.3 (b) illustrates the variation in apparent viscosity with increasing temperatures of 10 °C, 25 °C, and 50 °C. Notably, the sample treated with a 10 kGy γ-dose exhibits

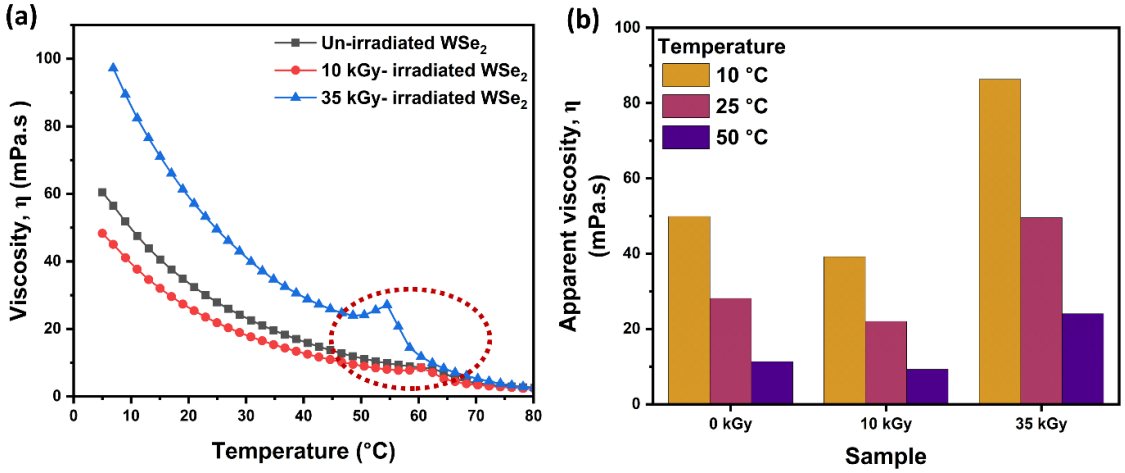

Figure 6.3: (a) Viscosity *vs.* temperature sweep plot at 5-80 °C of un-irradiated (0 kGy) and γ-irradiated at 10 kGy and 35 kGy of WSe_2/NaCMC nanocomposite solutions at a constant shear rate of 50 s^{-1}, (b) bar plot representing apparent viscosity at temperatures 10 °C, 25 °C, and 50 °C.

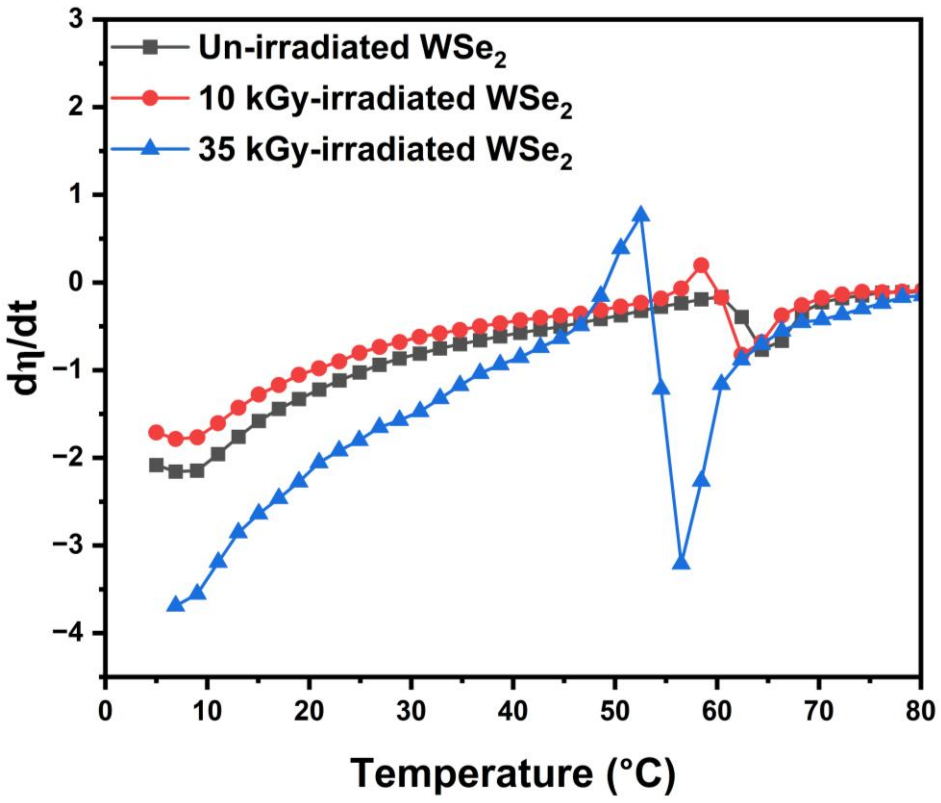

Figure 6.4: Derivative curve of viscosity with temperature of un-irradiated (0 kGy) and γ-irradiated WSe_2/NaCMC nanocomposite solutions at 10 kGy and 35 kGy.

comparatively lower apparent viscosity across these temperatures. As previously mentioned, a lower dose of γ-rays can also act as an exfoliating agent, producing thinner WS_2 layers and enhancing their dispersion within the polymer matrix, which in turn lowers the apparent viscosity of the nanocomposites. Additionally, to have a clear visualization of the glass transition temperature, the temperature dependence of viscosity was analyzed to acquire the corresponding derivative curve, as shown in Fig. 6.4. The temperature at which this derivative reaches a minimum is taken as the glass transition temperature [21]. Further, a noticeable shift toward lower temperatures is observed at a γ-dose of 35 kGy.

6.4 Effect of 15 keV He^{2+} ion irradiation on layered WSe_2

6.4.1 SRIM analysis

SRIM/TRIM calculations were carried out to determine the dominant energy loss mechanism, ion trajectories, 3D plots of ion distribution and total displacements that took

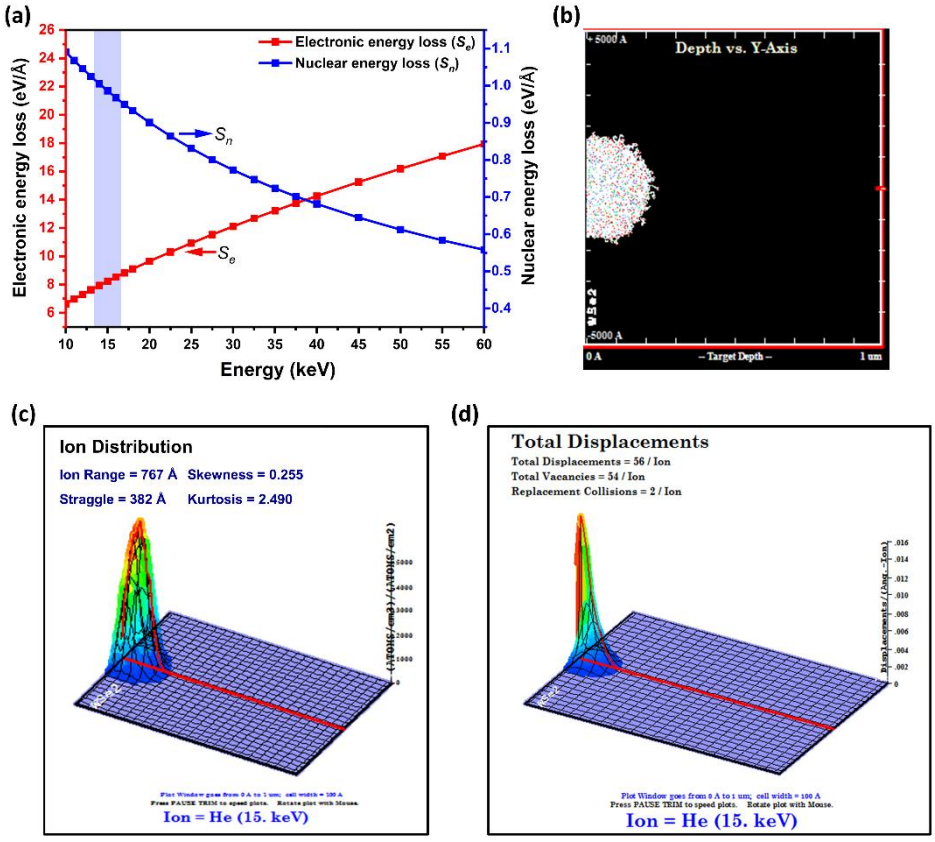

Figure 6.5: SRIM calculations of 15 keV He^{2+} ion irradiation on WSe_2 system (a) stopping power *vs.* energy plot in keV regime, (b) ion trajectories along target depth *vs*. y-axis, (c) ion distribution, and (d) total displacements plots occurred in the WS_2 system. Note that the plot window is considered up to a depth of 1 μm, as the incident ions penetrate from the left onto a target.

place due to the bombardment of 15 keV He^{2+} ion irradiation on WSe_2 material (Fig. 6.5 (a-d)). The electronic energy loss (S_e) and nuclear energy loss (S_n) caused by the 15 keV He^{2+} irradiation onto the WSe_2 system are ~8.24 eV/Å, and ~0.99 eV/Å, respectively. Their longitudinal and lateral straggling are calculated to be around 66.3 nm and 51.2 nm, respectively. The ion trajectories of the incident ions onto the target material, 3D plots for ion distribution range and total displacements, can be found in Fig. 6.5 (b-d). The projectile range of He ions stands at 76.7 nm, and the relevant 3D plots reveal that the He^{2+} irradiation was restricted to the near-surface region of the WSe_2 system.

6.4.2 Crystallographic and vibrational analysis

The powder XRD patterns of pristine and 15 keV He^{2+} ion irradiated WSe_2 systems at fluences ranging from 1×10^{15} to 1×10^{16} ions/cm^2 under normal incidence and at a fluence of 5×10^{15} ions/cm^2 under 55° oblique angle incidence are presented in Fig. 6.6(a). The diffraction peaks appear at ~13.83°, 41.94°, and 56.91°, corresponding to the (002), (006),

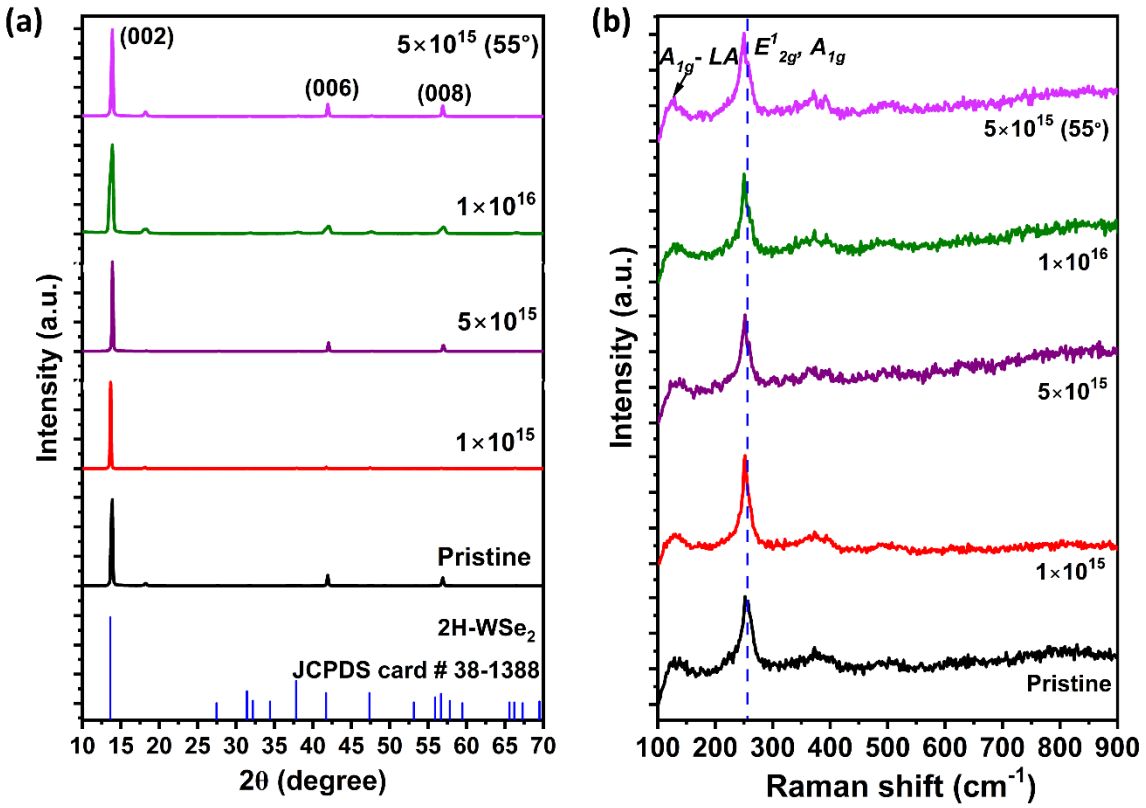

Figure 6.6: (a) X-ray diffraction patterns, and (b) Raman spectra of pristine WSe_2 (bulk) and after 15 keV He^{2+} ion irradiation at fluences 1×10^{15}, 5×10^{15}, and 1×10^{16} ions/cm^2 under normal incidences, and at a fluence of 5×10^{15} ions/cm^2 under oblique angle incidence.

Table 6.1. Lattice parameter and crystallite sizes estimation from powder-XRD analysis of 15 keV He^{2+} ion irradiated WSe_2 system.

Sl. No.	**Fluences (ions/cm^2)**	**Lattice parameter along *c*-axis direction (Å)**	**Crystallite size, d_c in 'nm'**
1	Pristine	12.82	31.3
2	1×10^{15}	12.96	46.9
3	5×10^{15}	12.73	45.1
4	1×10^{16}	12.85	16.1
5	5×10^{15} (55°)	12.78	29.3

and (008) crystallographic planes, as referenced in JCPDS card no. 38-1388 [13]. The powder XRD patterns corroborate with the hexagonal phase structure of WSe_2, which corresponds to the space group *P63/mmc* (no. 194). Notably, the prominent peak at around 13.83° is attributed to the unidirectional (002) plane, consistently present in all XRD patterns. The lattice parameters along the *c*-axis of the hexagonal phase WSe_2 structure, both pristine and irradiated with 15 keV He^{2+} ions, along with their average crystallite sizes (d_c) determined using Scherrer's law via Voigt curve fitting of the most intense (002) diffraction planes, are presented in Table 6.1. The crystallite size exhibits an unusual variation with fluence. As ion fluence increases, the WSe_2 structure initially undergoes grain growth from ~31.3 nm to 46.9 nm in the He^{2+} irradiated case, followed by a subsequent decrease. Similar observations have been reported in nanocrystalline ceria subjected to irradiation, as noted by P.D. Edmondson *et al*. [22], and V. Grover *et al.* [23]. These studies attribute the grain growth to defect accumulation caused by irradiation, referring to it as a defect-stimulated grain growth mechanism. Additionally, grain boundaries play a crucial role in limiting further grain growth. As a result, atomic displacements, structural disorder, and defect formation due to irradiation influence both interplanar spacings and the overall crystallinity of WSe_2 systems.

The Raman spectra of pristine WSe_2 and WSe_2 irradiated with 15 keV He^{2+} at fluences ranging from 1×10^{15} to 1×10^{16} ions/cm^2 under normal incidence, as well as at a fluence of 5×10^{15} ions/cm^2 under 55° oblique incidence, are shown in Fig. 6.6 (b). The first-order Raman modes, including the in-plane E^1_{2g} and out-of-plane A_{1g} modes, arise from vibrations between W-Se and Se-Se atoms in WSe_2. These modes exhibit a distinct sharp peak around 252 cm^{-1} due to degeneracy [14]. A redshift of approximately 2 cm^{-1} is observed at higher fluences in the E^1_{2g} /A_{1g} mode. Additionally, a Raman peak around ~136 cm^{-1}, attributed to the A_{1g}-LA combinatorial mode, becomes more pronounced with increasing fluence. No characteristic features of He^{2+} ions appear in the Raman spectra, as they are immiscible and tend to nucleate into bubbles, creating voids. Consequently, no new vibrational modes emerge in the irradiated system.

6.4.3 Inorganic fullerene (IF) like structure with He^{2+} irradiation

The morphological characteristics of both pristine and irradiated WSe_2, subjected to 15 keV He^{2+}, are analysed using HR-TEM imaging, as shown in Fig. 6.7. The morphology of pristine WSe_2 consists of dispersed flakes of WSe_2 sheets (Fig. 6.7 (a,b)). However, upon irradiation at a critical fluence of 5×10^{15} ions/cm^2, localised development of inorganic fullerene (IF)-like structures begins to emerge (Fig. 6.7 (c,d)). During low-energy ion irradiation, energy loss occurs as ions collide with atomic nuclei, triggering a secondary collision cascade. This cascade generates a high density of defects by displacing atoms from their lattice positions. In the case of helium ion exposure, these defects act as nucleation sites for helium bubbles. Due to the high mobility and low solubility of helium atoms, they migrate along grain boundaries, accumulating at trapping sites and eventually forming bubbles [24]. The formation of helium bubbles between the layers of the WSe_2 system weakens the van der Waals forces holding adjacent layers together, potentially leading to exfoliation and the formation of thinner layers. These weakly bonded thinner layers tend to curl due to the presence of the dangling bonds at the edges upon radiation exposure, eventually forming closed IF-like nanostructures. These nearly spherical IF-like structures lower the system's surface energy, increasing stability and rendering them thermodynamically inert [25]. Their average diameter ranges from ~30-50 nm, while the fringe width of these structures is around 0.33 nm, corresponding to the (110) plane of the hexagonal WSe_2 phase. Notably, these IF structures appear agglomerated and inseparable, forming many aggregates. Although these structures are generally inert due to the

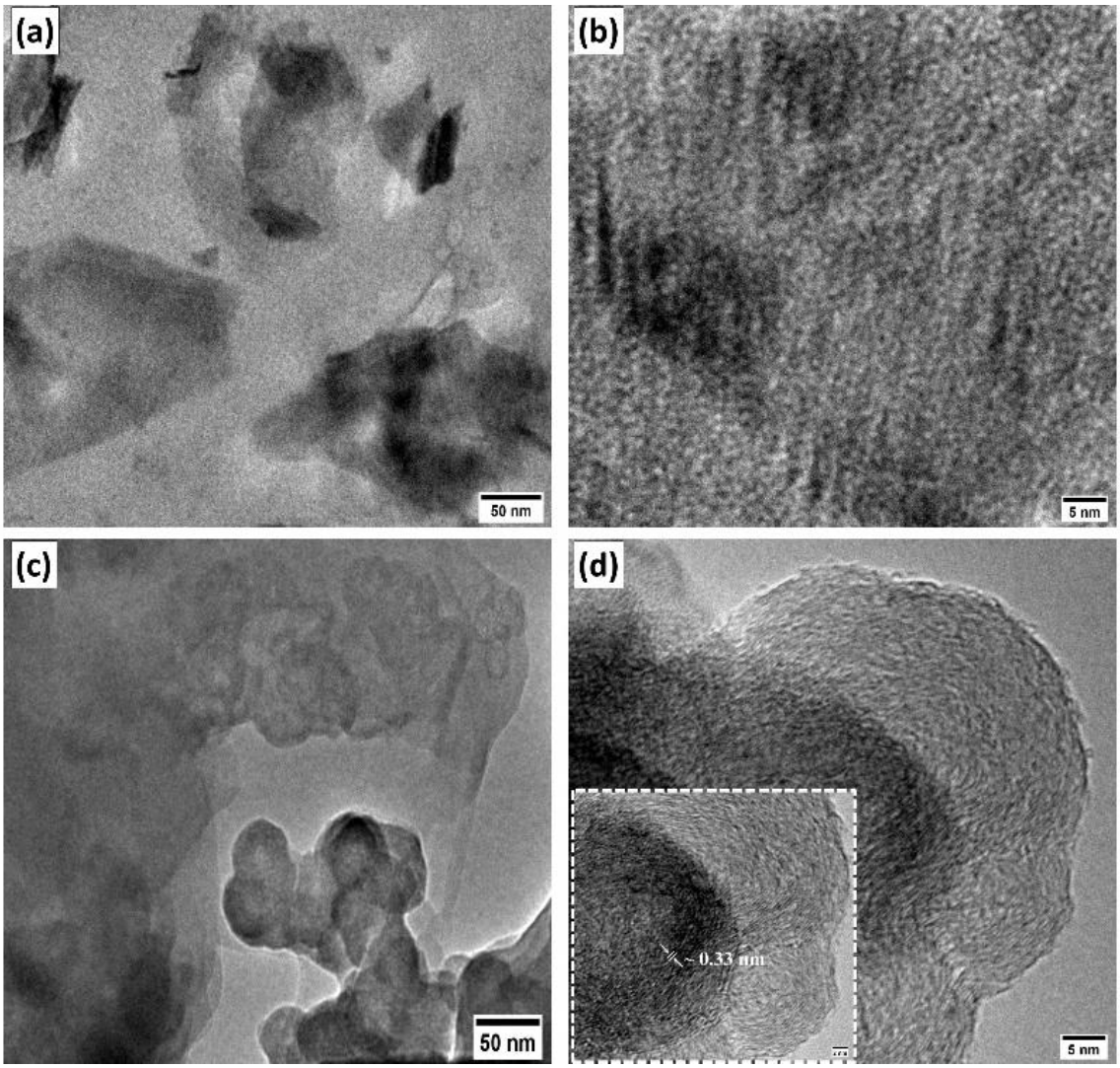

Figure 6.7: HRTEM images of (a,b) pristine WSe_2, and (c,d) after 15 keV He^{2+} ion irradiation at a fluence of 5×10^{15} ions/cm^2 under normal incidence with lower and higher magnified micrographs of scale bars 50 nm and 5 nm respectively, are shown; zoomed in image of inorganic fullerene-like structure with curved edges is shown as an inset in Fig. 6.7 (d).

saturation of dangling bonds, elastic strain and defects induced by surface curvature can lead to stronger adhesion between IF-nanostructures, causing them to agglomerate [26]. Unlike conventional fullerenes formed from carbon allotropes, the IF structures in WSe_2 possess closed spherical cages [27]. These IF-like nanostructures exhibit excellent self-lubricating properties, making them highly suitable for various applications, including polymer-based coatings [28, 29].

6.5 Effect of 15 keV C^{2+} ion irradiation on layered WSe_2 nanosystems

6.5.1 SRIM analysis

SRIM/TRIM calculations reveal that the dominant energy loss mechanism of 15 keV C^{2+} ions in the WSe_2 system primarily occurs through energy losses of S_e and S_n, with values of ~12.68 eV/Å and 9.30 eV/Å, respectively (Fig. 6.8 (a)). Furthermore, C^{2+} ion irradiation primarily affects the near-surface region of WSe_2, with a projectile range of around 24.5 nm. The longitudinal and lateral straggling are estimated to be ~27.0 nm and ~20.2 nm, respectively. The ion trajectories within the target material, along with 3D plots illustrating ion distribution range and total displacements, are presented in Fig. 6.8 (b-d).

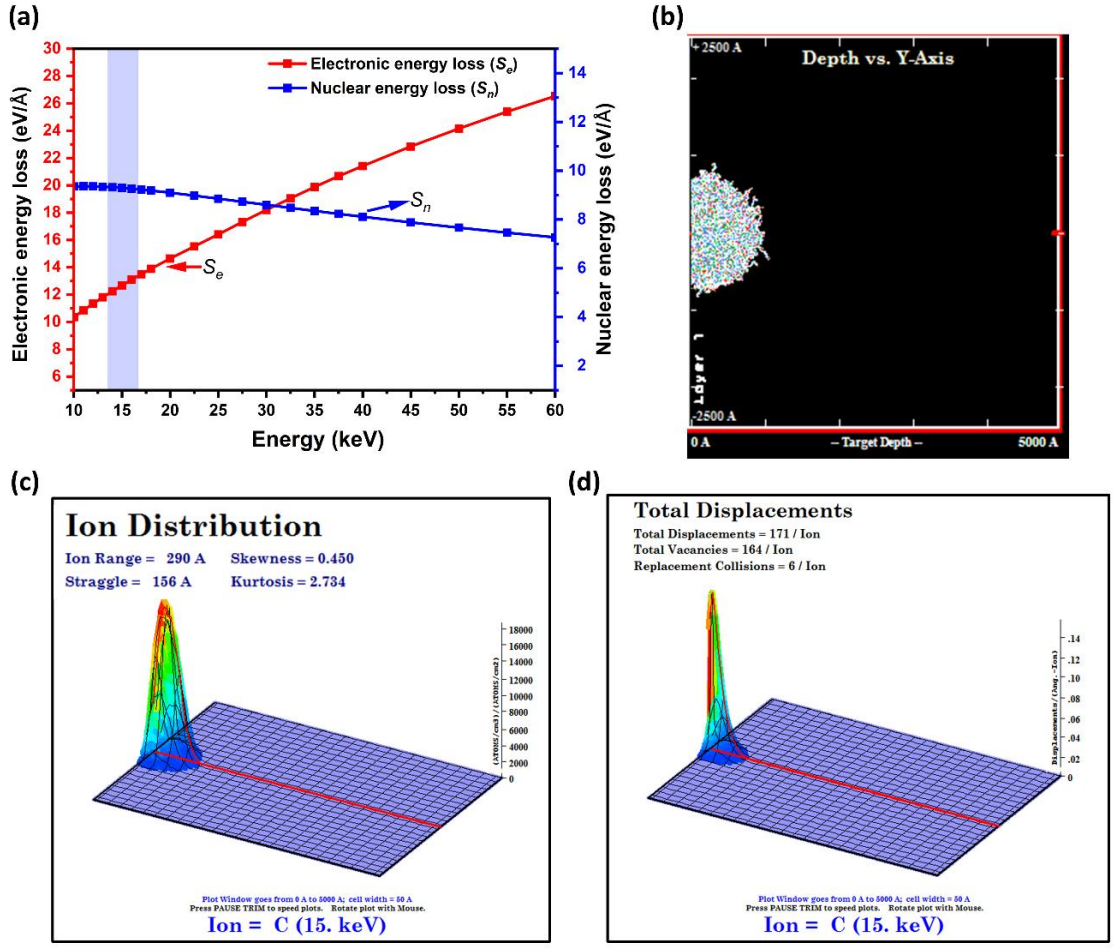

Figure 6.8: (a) SRIM calculations of 15 keV C^{2+} ion irradiation on exfoliated WSe_2 system (a) stopping power *vs.* energy plot in keV regime, (b) ion trajectories along target depth *vs*. y-axis, (c) ion distribution, and (d) total displacements plots occurred in the WSe_2 system. Note that the plot window is considered up to a depth of 5000 Å, as incident ions penetrate from the left onto a target.

6.5.2. Phase structure and vibrational analysis

The XRD patterns of exfoliated WS_2 in pristine form and irradiated with 15 keV C^{2+} ions at fluences 1×10^{15}, 3.5×10^{15}, 7.5×10^{15} and 1×10^{16} ions/cm^2 at normal incidence can be found in Fig. 6.9 (a). The diffraction patterns were acquired in the range of Bragg's angle, 2θ ~10º-70º. They exhibit 2θ values positioned at ~13.84°, 41.84°, and 57.09°, coinciding with the (002), (006), and (008) diffraction planes of the WSe_2 material. XRD patterns reveal that these results align with the hexagonal phase structure of the WSe_2 system, which is associated with the space group (*P63/mmc*, no. 194). The profound peak at around ~13.83° is associated with the unidirectional (002) plane that emerged in all the XRD patterns. The lattice parameters along the *c*-axis of the WSe_2 hexagonal phase structure of pristine WSe_2 and irradiated with 15 keV C^{2+} ions, along with their average crystallite size (d_c), are presented in Table 6.2.

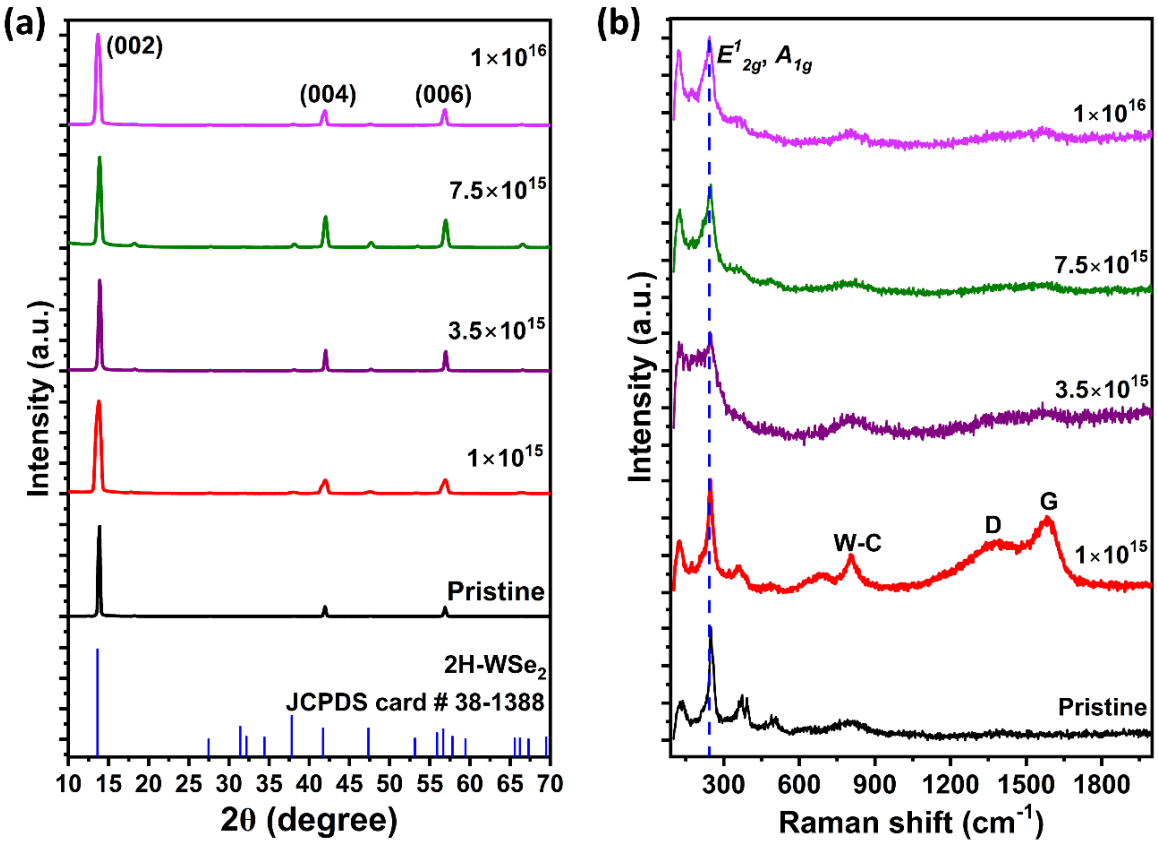

Figure 6.9: (a) XRD patterns, and (b) Raman spectra of pristine WSe_2 (exfoliated) and after 15 keV C^{2+} ion irradiation at fluences 1×10^{15}, 3.5×10^{15}, 7.5×10^{15}, and 1×10^{16} ions/cm^2 under normal incidences.

Table 6.2. Lattice parameter and crystallite sizes estimation from the acquired XRD patterns of 15 keV C^{2+} ion irradiation on exfoliated WSe_2.

Sl. No.	**Fluence (ions/cm^2)**	**Lattice parameter along *c*-axis direction (Å)**	**Crystallite size, d_c in 'nm'**
1	0 (Pristine)	12.81	28.2
2	1×10^{15}	12.91	11.7
3	3.5×10^{15}	12.81	19.7
4	7.5×10^{15}	12.78	14.0
5	1×10^{16}	12.93	14.4

Raman spectra of pristine and C^{2+} ion irradiated WSe_2 in the exfoliated form are shown in Fig. 6.9 (b). In addition to the notable vibrational E^1_{2g}, A_{1g} modes of ion-irradiated WSe_2, the Raman spectra exhibit the emergence of the *LA* mode at ~122 cm^{-1}, specifying the existence of defects. The intensity of this defect-induced *LA* mode tends to increase with higher ion fluences. In addition, the Raman spectra at a critical fluence of 1×10^{15} ions/cm^2 show noticeable *D* and *G* bands appearing near 1393 cm^{-1} and 1587 cm^{-1}, respectively. Here, a weak *D* band appears owing to the presence of defects such as vacancy, edge, etc. and is linked with the intervalley double resonant process, while the *G* band corresponds to carbon-based material [30]. This can profoundly alter the electronic properties of the host material. Furthermore, the peak at ~802 cm^{-1} represents the characteristic vibrational mode of the W-C bond present in the irradiated WSe_2 material. Nevertheless, at a critical fluence of 1×10^{15} ions/cm^2, the emergence of these two bands is a signature of C implanted in the WSe_2 system through 15 keV C^{2+} ion irradiation at a particular fluence.

6.5.3. Morphological modification and sheet fragmentation with C^{2+} irradiation

The morphological analysis of pristine WSe_2 can be found in Fig. 6.10 (a). The imaging shows sheets of WSe_2 having fringe width with an interlayer *d*-spacing value of around ~0.60 nm (Fig. 6.10 (b)). This is consistent with the (002) plane of the WSe_2 hexagonal crystal structure. The irradiated WSe_2 systems at fluences 1×10^{15} ions/cm^2 and 1×10^{16} ions/cm^2 show fragmented sheets of uneven sizes with C^{2+} ion irradiation (Fig. 6.10 (c)). The interlayer spacing after irradiation at low fluence is calculated to be ~0.68 nm, depicted in Fig. 6.10 (d). This also corresponds to the (002) crystallographic plane of the hexagonal WSe_2 phase with little expansion compared to the pristine case. The TEM imaging at the highest fluences, though unclear, shows some patches of C-dots. This observation is further supported by the EDX spectra and the corresponding weight and atomic percentages of W, S, C, and O shown in Fig. 6.11 (a, b). Particularly, the carbon signal is comparatively stronger compared to the pristine system, suggesting the incorporation of carbon into the WSe_2 system with an increase in atomic % from 38.2 % to 73.8 % as a result of C^{2+} irradiation. The presence of both carbon and oxygen is also considered in the pristine system also, as these elements can appear as traces due to exposure to the environment.

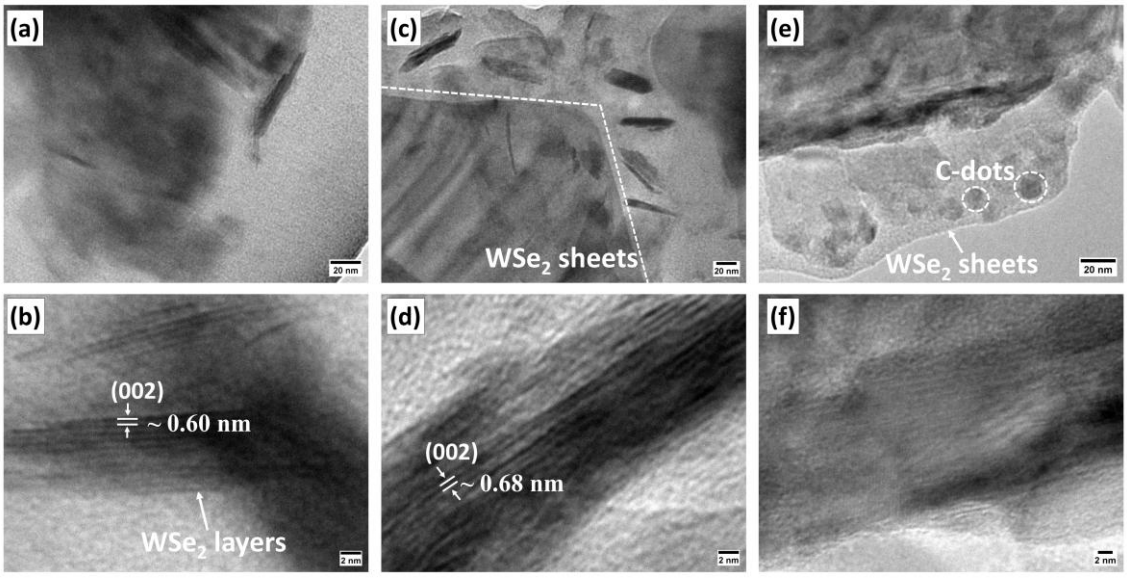

Figure 6.10: HRTEM images of (a,b) pristine (exfoliated WSe_2), and after 15 keV C^{2+} ion irradiation at a fluence of (c,d) 1×10^{15} ions/cm^2, (e,f) 1×10^{16} ions/cm^2 at normal incidences with lower as well as higher magnification of scale bars 20 nm and 2 nm, respectively.

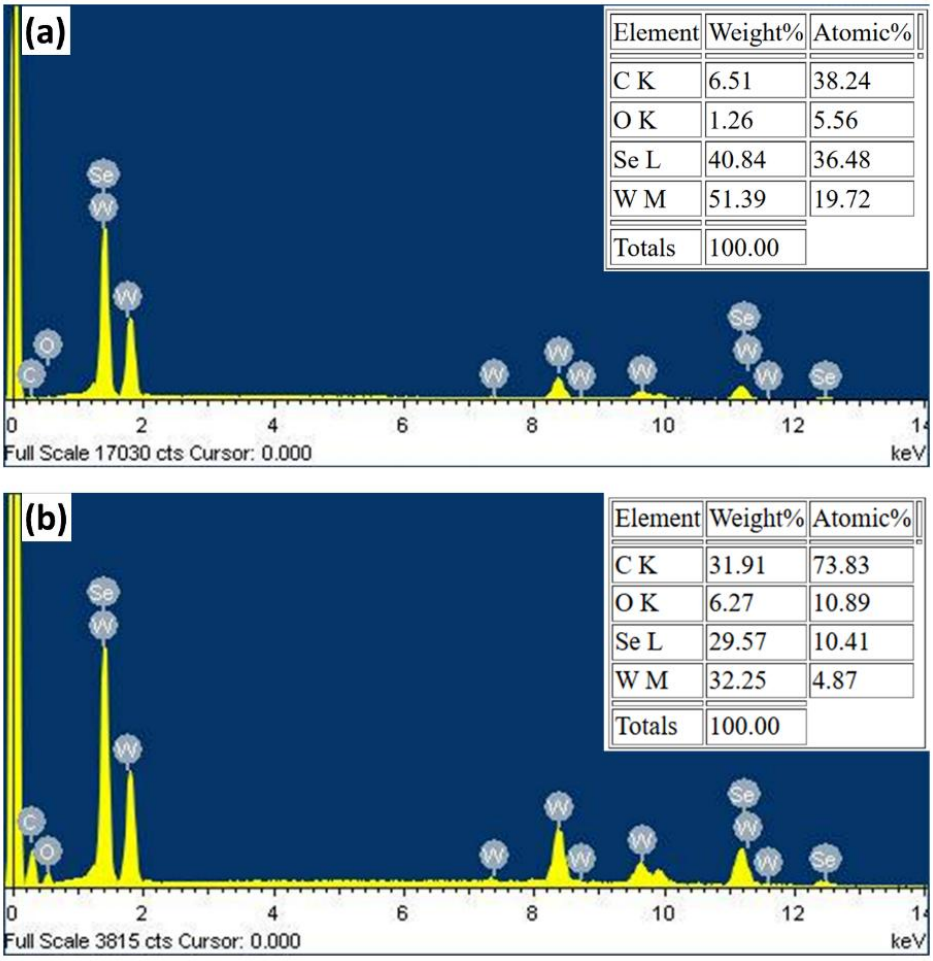

Figure 6.11: EDX spectra of (a) pristine and (b) irradiated WSe_2 with 15 keV C^{2+} irradiation at a fluence of 1×10^{16} ions/cm^2.

6.6 Effect of 60 MeV N^{5+} ion irradiation on exfoliated WSe_2 systems

6.6.1 SRIM calculations

SRIM calculations were performed to understand the primary mechanisms influencing the ion path and interaction of 60 MeV N^{5+} ions within the targeted WSe_2 material. The results determine that the electronic energy loss ($S_e \approx 167.8$ eV/Å) is significantly greater than the nuclear energy loss ($S_n \approx 0.11$ eV/Å), as shown in Fig. 6.12 (a). Additionally, the projected range of ions is estimated where incident ions penetrate the material up to a depth of ~27.89 µm, with lateral and longitudinal straggling values of around ~1.15 µm and ~1.09 µm, respectively. A schematic illustration of the ion irradiation event on exfoliated WSe_2 is provided in Fig. 6.12 (b), offering an abstract view of the ion-matter interaction.

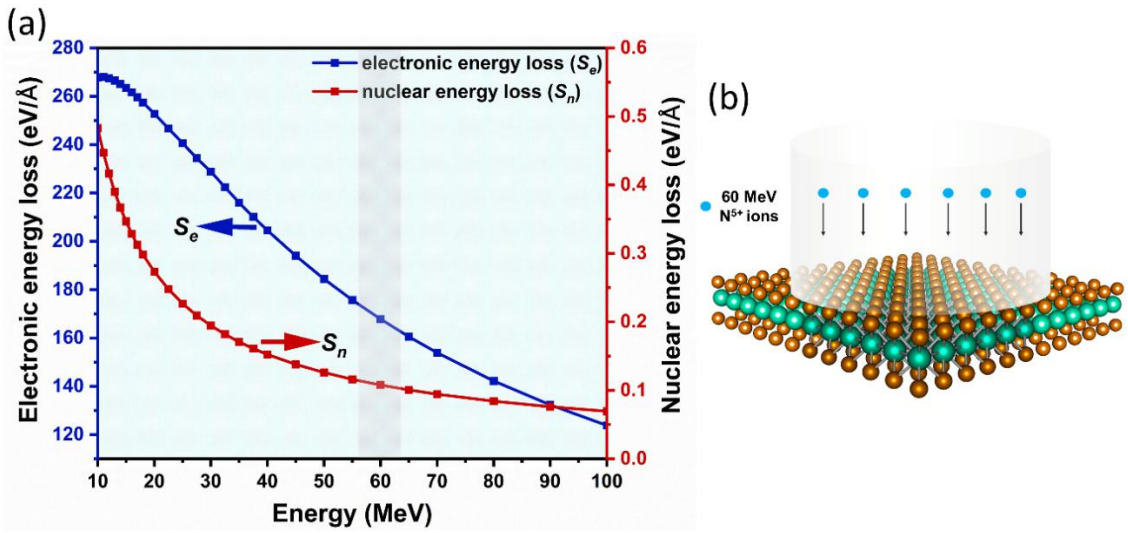

Figure 6.12: SRIM/TRIM calculation for 60 MeV N^{5+} ion irradiation: (a) stopping power *vs.* energy plot for N^{5+} ions bombarded onto WSe_2 material, (b) schematic illustration of the SHI irradiation on WSe_2 material with N^{5+} ion beam.

6.6.2 Structural analysis

The XRD patterns of both pristine and 60 MeV N^{5+} ion-irradiated WSe_2 samples are shown in Fig. 6.13 (a). The dominant diffraction peaks correspond to the 2H-WSe_2 phase, associated with the hexagonal structure (space group *P63/mmc*). Notably, the post-irradiation XRD patterns show no additional peaks, indicating that the phase purity and crystalline structure of WSe_2 remain preserved even after ion exposure. No signs of amorphization were observed, even at the highest fluence of 5×10^{13} ions/cm^2. The characteristic peaks appearing at 2θ values of ~13.5°, 41.2°, and 56.3° are indexed to the (002), (006), and (008) crystallographic planes, respectively, in accordance with JCPDS card no. 38-1388 [31]. The average crystallite size (d_c) was determined using single-line Voigt fitting of the (002) diffraction peak, based on Scherrer's equation, with the corresponding values summarized in Table 6.3. Notably, d_c exhibits an unusual trend with increasing ion fluence. Initially, the average crystallite size increases, reaching ~44 nm at a fluence of 1×10^{12} ions/cm^2, suggesting particle growth. However, at a higher fluence of 1×10^{13} ions/cm^2, the size drops to ~27 nm. This reduction may be attributed to the formation of irradiation-induced defects, such as edge dislocations caused by ion impacts at grain boundaries, which can hinder particle growth [22]. Again, at the highest fluence, the crystallite size increases to about 60 nm. This could result from structural reorganization of the lattice atoms, resulting in recrystallization in the irradiation process.

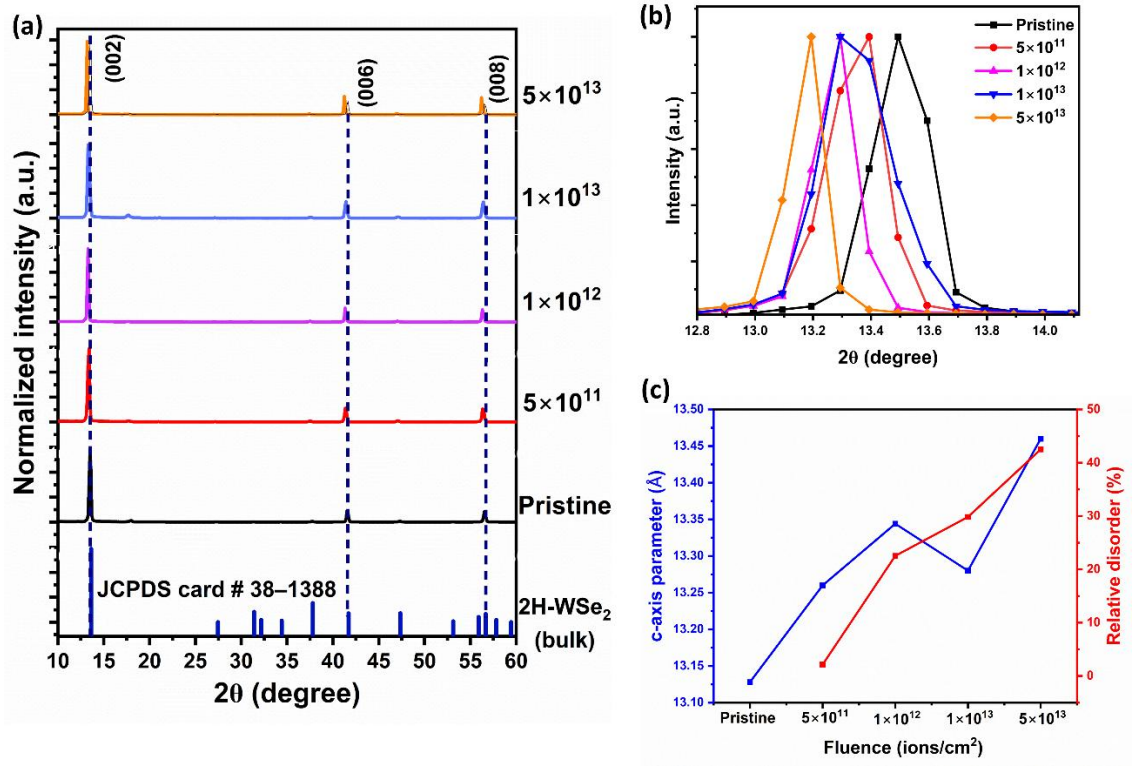

Figure 6.13: (a) A series of XRD patterns, (b) zoomed plot of (002) peak oriented along *c*-axis direction, (c) plot showing variations in the *c*-axis parameter and damage estimated with ion fluences of 60 MeV N^{5+} ion irradiation in WSe_2.

Table 6.3. Structural parameters of exfoliated WSe_2 subjected to 60 MeV N^{5+} irradiation.

Sl. No.	Fluence (ions/cm^2)	Lattice parameter (Å) along the *c*-axis	Average crystallite size, d_c (nm)	FWHM of (002) peak	Relative change in the FWHM of the (002) peak	Disorder (%)
1	Pristine	13.1	34	0.23	-	-
2	5×10^{11}	13.3	34	0.24	0.01	02.2
3	1×10^{12}	13.3	44	0.18	0.05	22.5
4	1×10^{13}	13.3	27	0.30	0.07	29.8
5	5×10^{13}	13.5	60	0.13	0.10	42.5

Furthermore, the exfoliated pellets may hold WSe_2 flakes oriented in various directions, featuring different radiation-assisted conditions for the dislodgement of host atoms.

Additionally, irradiation-induced disorder can be evaluated through the broadening of XRD peaks. This is measured by the relative change in the full width at half maximum (FWHM) of the (002) peak compared to the pristine case (Fig. 6.13 (b)). The extent of lattice distortion due to irradiation and hence the disorder is estimated using equation (5.4) mentioned in the previous chapter [32]. The analysis shows a monotonic increase in disorderness in the lattice structure due to bombardment of N^{5+} ions with increasing ion fluence in the studied system. Also, an increase in the values of lattice parameters along the *c*-axis direction reveals lattice expansion of the WSe_2 system along that particular orientation after irradiation, as evident from Table 6.3 and Fig. 6.13 (c). The observable lattice expansion, particularly at the highest fluence of N^{5+} irradiation, results in a lowering of the 2θ value [23].

6.6.3 Vibrational analysis

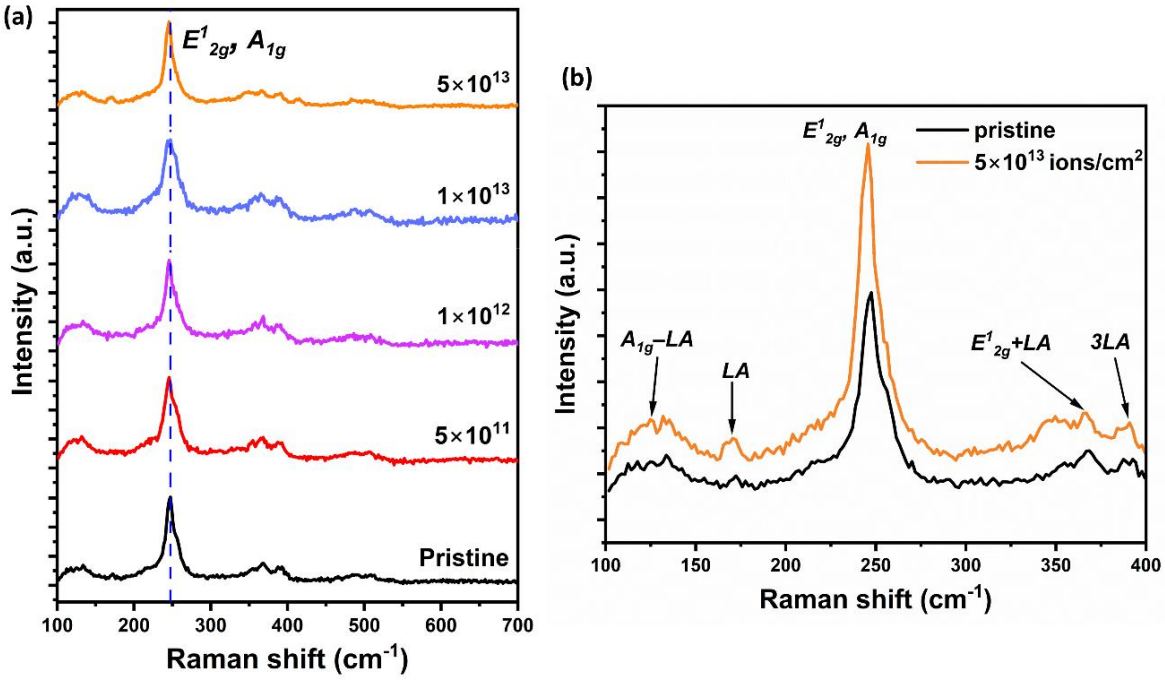

Figure 6.14: Raman spectra before (pristine) and after irradiation of the WSe_2 system at fluences 5×10^{11}, 1×10^{12}, 1×10^{13} and 5×10^{13} ions/cm^2, respectively, and (b) Raman modes are assigned with an enlarged plot shown for pristine and at the highest fluence (5×10^{13} ions/cm^2).

The Raman active optical phonon modes of pristine and 60 MeV N^{5+} ion irradiated WSe_2 are shown in Fig. 6.14 (a). The prominent, zone-centre first-order in-plane E^1_{2g} mode of WSe_2 material is evident at ~247 cm^{-1}, and the out-of-plane, A_{1g} vibrational mode exists in the vicinity [33]. The slight asymmetry in the right-hand shoulder of the noticeable E^1_{2g} mode signifies the presence of the A_{1g} mode. In addition, some multi-phonon scattering peaks, or bands, appear involving the longitudinal acoustic (*LA*) mode due to the second-order Raman process discussed in *Section 6.3.1* of this chapter. In this regard, a combinatorial A_{1g}-*LA* mode is observed at ~134 cm^{-1} with a broadened feature in the lower wavenumber region of the spectra. Moreover, at the higher wavenumber region, the mixed mode arises due to the combined process at ~367 cm^{-1} and is attributed to the E^1_{2g}+*LA* mode. The weakly resolved peak at ~391 cm^{-1} corresponds to the 3*LA* mode, which is a third-order resonant Raman mode [34–36]. Apart from this, a minute peak near ~170 cm^{-1} reveals structural disorder in the material represented by the *LA*(*M*) mode, which appears as a very low-intensity peak visible at the highest fluence. The augmented vibrational responses of the E^1_{2g} and the *LA* modes are noticeable for the irradiated WSe_2 as compared to its pristine counterpart, shown in Fig. 6.14 (b).

6.6.4 Morphological analysis

AFM and TEM analyses were executed to further investigate the changes in the morphology and microstructures of the irradiated WSe_2 at higher fluences. The surface morphology, along with its respective 3D topography, representing sheets of the WSe_2 material for pristine and 60 MeV N^{5+} irradiated WSe_2 systems at a fluence of 5×10^{13} ions/cm^2, can be found in Fig. 6.15 (a-d). The irradiated specimen characterizes rougher surfaces by the presence of agglomerated stacks of sheets of 2D surfaces, offering a root mean square (RMS) roughness value of ~146.1 nm. This is nearly 1.5 times increase in surface roughness due to irradiation as compared to the pristine case, which stands at a roughness value of ~95.4 nm.

Through TEM imaging, surface modification could be observed after irradiation, along with sheet-like morphologies of the pristine WSe_2 material (Fig. 6.16 (a-d)). In addition, voids and damaged regions marked in red are quite apparent after SHI impact at a higher fluence. The fast Fourier transform (FFT) patterns obtained from the marked regions of yellow dashed squares in Fig. 6.16 (c,d) are shown as insets. The region containing voids exhibits a diffuse halo ring in the FFT pattern (Fig. 6.16 (c)), indicative

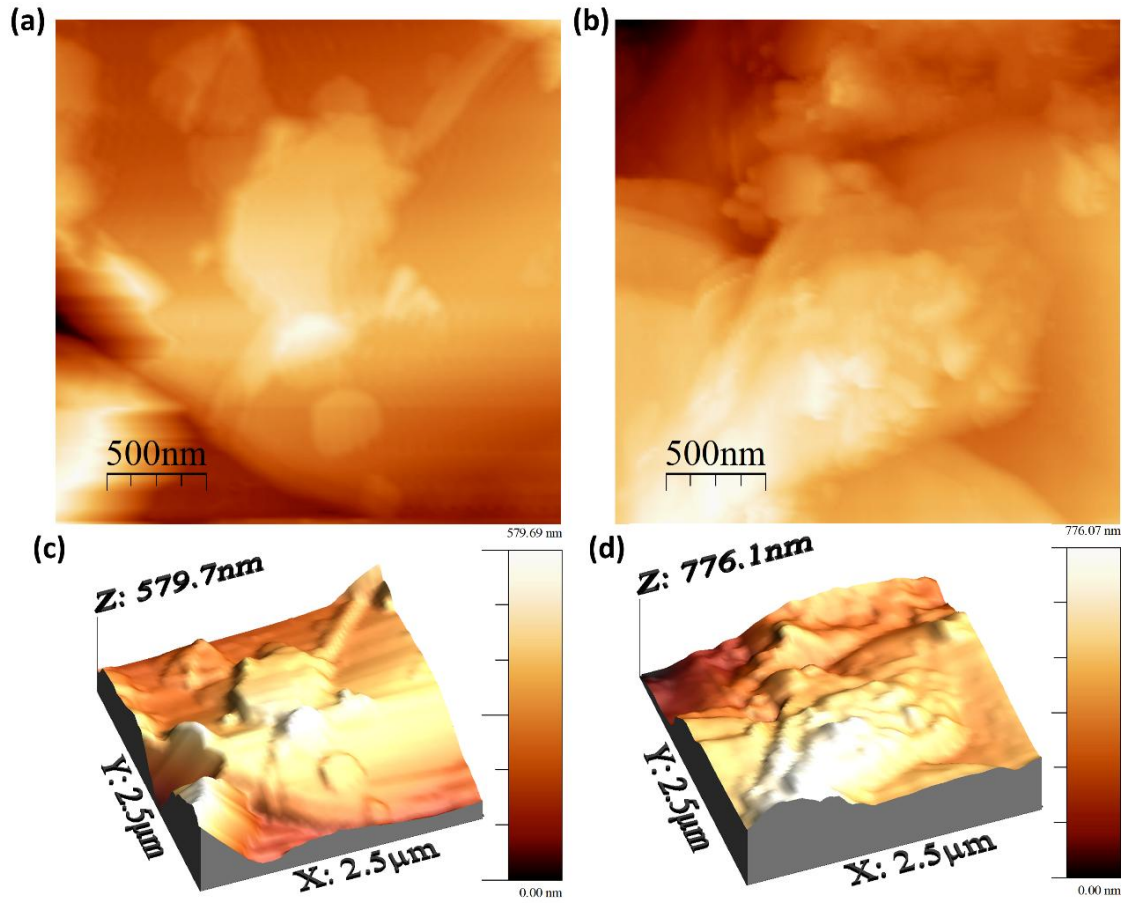

Figure 6.15: AFM images of 2D surface scans of (a) pristine (exfoliated WSe_2) and after irradiation for fluences (b) 5×10^{13} ions/cm^2, and (c, d) corresponding 3D topographies are shown.

of structural defects or disorder induced by irradiation. In contrast, the FFT patterns from the fringe regions, as shown in Fig. 6.16 (d), display distinct diffraction spots. Furthermore, the interlayer *d*-spacing values were estimated from the observable lattice fringes and found to be ~0.60 nm for pristine WSe_2, increasing to about 0.64 nm after irradiation with 60 MeV N^{5+} ions. This expansion is attributed to structural disorder induced by ion irradiation, which is also supported by the observed shift toward lower 2θ values in theXRD patterns with increasing ion fluence (Fig. 6.16 (b, d)). In particular, these interlayer spacings correspond to the (002) crystallographic planes of WS_2, as discussed in *Section 6.6.2*. Additionally, the SAED pattern in Fig. 6.16 (e) offers diffused rings with continuous bright spots in the case of the pristine system. In contrast, the distinct bright spots reveal that the crystallinity of the WSe_2 material has improved after radiation exposure at a fluence 1×10^{13} ions/cm^2 (Fig. 6.16 (f)).

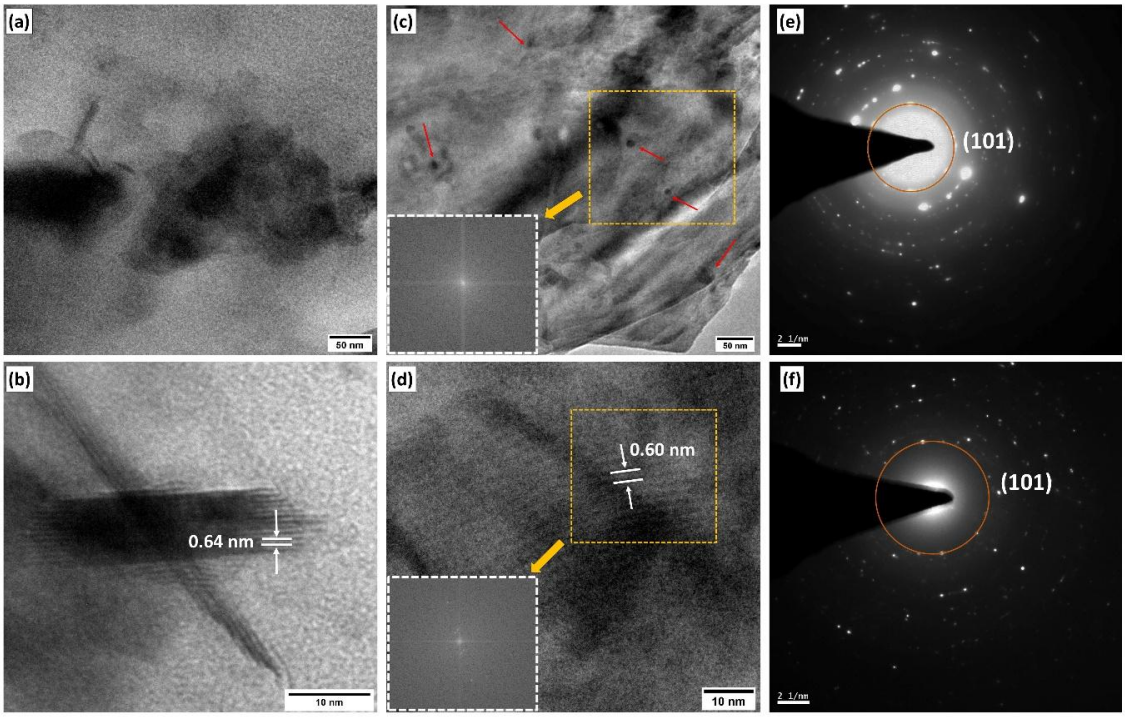

Figure 6.16: HR-TEM imaging of (a,b) pristine WSe_2, (c,d) at fluence 1×10^{13} ions/cm^2 at lower as well as higher magnification along with FFT patterns of marked regions shown as an insets, (e,f) SAED pattern of pristine WSe_2 and 60 MeV N^{5+} ion irradiation in WSe_2 material. Note that the scale bars shown are 50 nm and 10 nm, respectively.

6.6.5 Computational details

In the context of SHI irradiation, where high-energy particles collide with the target material, the likelihood of forming clusters of point defects (particularly, chalcogen vacancies) increases substantially [37]. So, a computational study was performed by considering a cluster of defects or vacancies in the WSe_2 system. To model the system, a 4×4 supercell of the WSe_2 monolayer was employed, consisting of 16 W and 32 Se atoms lying across the *x*-*y* plane (Fig. 6.17 (a)). To create a vacancy cluster, a W atom along with two associated Se atoms was removed from the supercell. These two Se atoms were originally bonded to the removed W atom (Fig. 6.17 (b)). To ensure minimal interaction between layers in the perpendicular direction, a spacing of 15 Å was introduced along the *z*-axis of the system. Due to constraints arising from the number of atoms in a supercell and the need to preserve a consistent defect concentration throughout the computational study, the monolayer configuration of WSe_2 was chosen. The computations were executed using first-principles methodology and density functional theory, employing a plane-wave

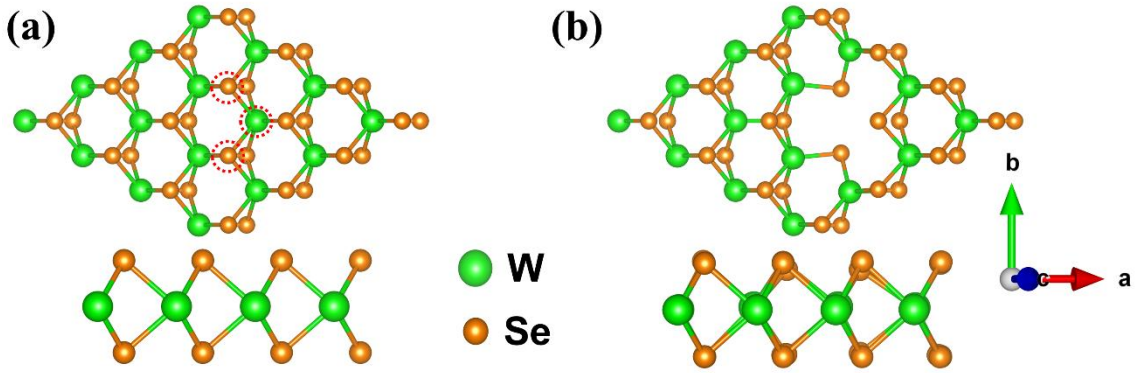

Figure 6.17: Optimized structure of 4×4 supercell of (a) pristine WSe_2, (b) WSe_2 monolayer with vacancy cluster (the top view is tilted by 15° along the perpendicular direction of the plane). The red dotted circles in (a) indicate the removed atoms to create the vacancy cluster in (b).

basis set within the QUANTUM ESPRESSO framework [38–41]. Norm-conserving scalar relativistic (NC-SR) pseudopotentials were applied, with a dense Monkhorst k-grid of 5×5×1 for self-consistent field calculations and 10×10×1 for non-self-consistent field calculations. The Perdew-Burke-Ernzerhof (PBE) exchange-correlation functional, incorporating the generalized gradient approximation (GGA), was consistently utilized [42]. Parameters such as the kinetic energy cutoff and charge density cutoff were set at 680 eV and 4081 eV, respectively. Structural relaxation was allowed until a force convergence threshold of 10^{-3} Ry/Bohr was met. The convergence criteria for the self-consistent calculations were uniformly set at 10^{-6} Ry for all modelled structures.

6.6.6 Electronic properties of defect clusters

In reference to the formation of a vacancy cluster, the energy required in the formation of a W or a Se vacancy in the WSe_2 lattice is calculated using the following formula [43],

$$E_{vf} = E_D - E_P + \mu_{W/Se} \tag{6.3}$$

here, E_D represents the total ground state energies of the WSe_2 monolayer with a W or Se vacancy; and E_P denotes the total ground state energy of pristine WSe_2. The term $\mu_{W/Se}$ is the chemical potential of the removed W or Se atom. The calculated formation energy for a W and Se vacancy are found to be ~5.3 eV and ~2.63 eV, respectively. This finding aligns well with previous results for WSe_2 monolayers [44]. Notably, these formation energies suggest that the energy required to eliminate a W atom could easily remove two Se atoms from the WSe_2 surface. In addition, Yang *et al*., in their investigation of various

vacancy types in WSe_2, also demonstrated that the formation energy for two Se atoms (5.39 eV) is nearly equal to that of a single W atom vacancy (5.35 eV) [44].

To examine the influences of SHI irradiation on the electronic structure of layered WSe_2, a monolayer of the few-layer system was considered featuring a combination of two selenium (Se) vacancies in proximity to the W vacancy. The ratio of 2:1 for Se and W vacancies is chosen, taking their respective formation energies into account. In its monolayer form, WSe_2 has been reported to exhibit a direct band gap at the *K* point in the Brillouin zone (BZ) [45]. However, Wei-Ting *et al*. demonstrated that under unstrained conditions, the WSe_2 monolayer actually features an indirect band gap, with its valence band maxima (VBM) at the *K*-point and the conduction band minima (CBM) at the *Q* point along the *K*-*Γ* direction. The computational analysis reveals that the indirect band gap of the material is situated at the *K*-*Q* point of the BZ and is 1.48 eV (Fig. 6.18 (a) and 6.18 (c)). The direct band gap of the material is 1.61 eV at the *K*-point of the BZ. This finding is in agreement with the report by Wei-Ting *et al.* [46]. Consistent with the earlier reports, the optimized lattice parameters and the average W-Se bond length of the WSe_2 unit cell are found to be 3.32 Å and 2.55 Å, respectively [47, 48]. However, the introduction of a vacancy cluster in the supercell causes a contraction in the average bond length of W-Se near the defect site, shrinking it to 2.45 Å. These spatial modifications give rise to numerous localized defect states within the forbidden gap of the monolayer, thereby inducing a transitional shift in its electronic structure. The defect state lying right above the Fermi level has its conduction band minima at the *Γ*-point, and the band right below the Fermi level has its valence band maxima lying at the *K*-point. Owing to these defect states within the forbidden gap, the band gap of the monolayer, having a cluster of vacancy defects, decreases to ~0.37 eV along the *K*-*Γ* direction in the BZ (Fig. 6.18 (b)). The monolayer with the vacancy cluster has a competing direct band gap at the *K*-point of ~0.39 eV. These defect states manifest in both the conduction and valence bands, as depicted in Fig. 6.18 (b) and Fig. 6.18 (d). The defect states on both sides of the Fermi level are ascribed to the Se 4*p* and W 5*d* orbitals (Fig. 6.18 (d)). The symmetric nature of spin up and spin down states in Fig. 6.18 (b) and Fig. 6.18 (d) indicates that the vacancy cluster would induce zero magnetic moments in the monolayer and thus, retain the non-magnetic nature of its pristine counterpart.

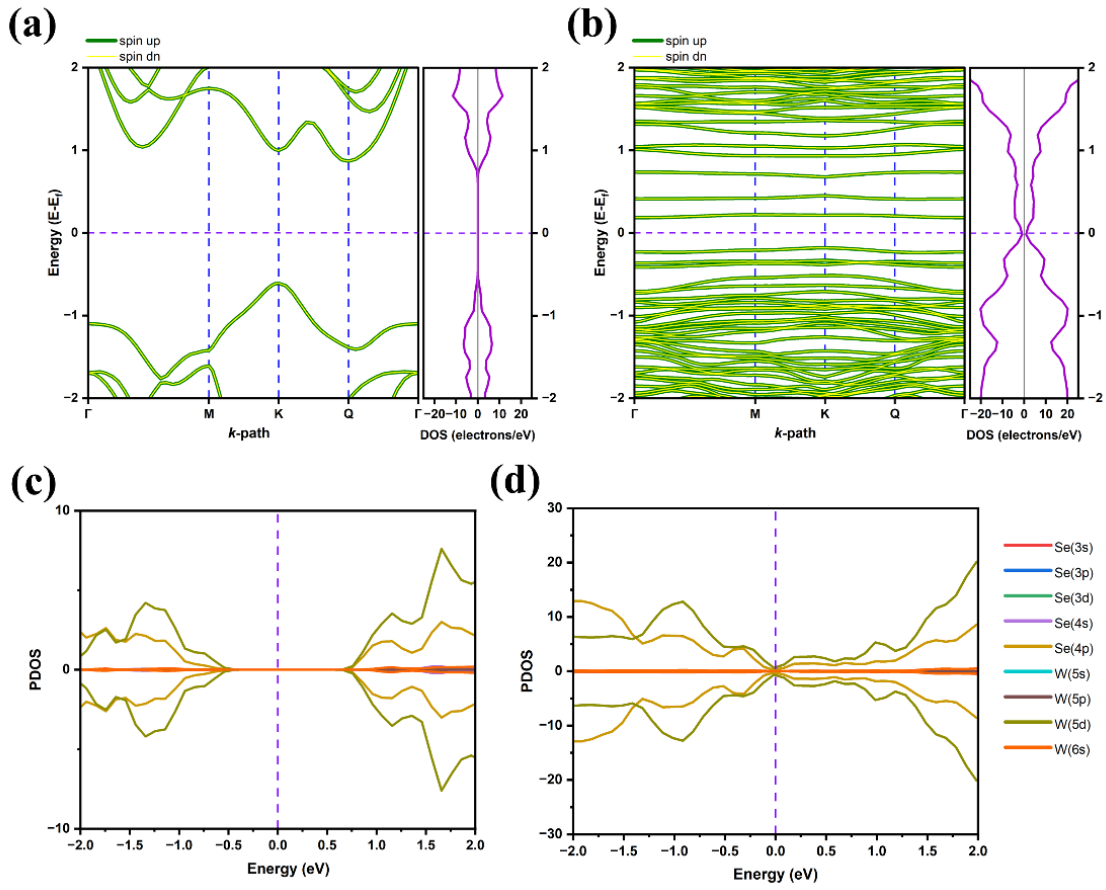

Figure 6.18: Electronic band structure and projected density of states (PDOS) of (a,c) pristine WSe_2, and (b,d) WSe_2 with a vacancy cluster, respectively. The spin-up states are indicated by the green-coloured bands, and the spin-down state is represented by the yellow-colored lines of the band structures.

6.7 Concluding remarks

In conclusion, the ion irradiation technique plays a crucial role in tailoring the properties of materials. This chapter explores the effect of γ-irradiation, 15 keV He^{2+}, 15 keV C^{2+} ions, and high-energy 60 MeV N^{5+} ions on the WSe_2 system. The phase structure and crystallinity of WSe_2 remain intact even at higher ion fluences after irradiation impact. Notably, the γ-irradiated WSe_2 was incorporated into a NaCMC polymeric solution to study its rheological properties, particularly in a 1 wt.% nanocomposite solution. The flow curves of these WSe_2/NaCMC nanocomposites follow a non-Newtonian behaviour with a shear-thinning trend, characterized by a power-law index (*m*) between 0.84 and 0.86 in a shear rate range of 0-1000 s^{-1}. For He^{2+} ion irradiation, at a fluence of 5×10^{15} ions/cm^2 under normal incidence (0°), closely packed spherical inorganic fullerene (IF)-like structures are observed in WSe_2. In the case of 15 keV C^{2+} ion exposure, Raman

spectroscopy reveals the appearance of D and G bands, indicating carbon atom implantation into the WSe_2 system. Meanwhile, irradiation with 60 MeV N^{5+} ions led to a substantial increase in surface roughness, with AFM analysis showing a post-irradiation RMS roughness of ~146 nm at the highest fluence. TEM images further confirm morphological changes, displaying layered sheets interspersed with voids. First-principles calculations based on vacancy clusters in WSe_2 are studied, demonstrating the tunable bandgap, highlighting the potential for controlled electronic property modifications. This tunability opens up intriguing possibilities for engineering new functionalities in future device applications.

References

[1] Cho, K., Pak, J., Chung, S., Lee, T. Recent Advances in Interface Engineering of Transition-Metal Dichalcogenides with Organic Molecules and Polymers. *ACS Nano*, *13*(9): 9713–9734, 2019.

[2] Zhou, H., Wang, C., Shaw, J.C., Cheng, R., Chen, Y., Huang, X., Liu, Y., Weiss, N.O., Lin, Z., Huang, Y., Duan, X. Large Area Growth and Electrical Properties of p-Type WSe_2 Atomic Layers. *Nano Letters*, *15*(1): 709–713, 2015.

[3] Cheng, Q., Pang, J., Sun, D., Wang, J., Zhang, S., Liu, F., Chen, Y., Yang, R., Liang, N., Lu, X., Ji, Y. WSe_2 2D p-type semiconductor-based electronic devices for information technology: design, preparation, and applications. *InfoMat*, *2*(4): 656–697, 2020.

[4] Eftekhari, A. Tungsten dichalcogenides (WS_2, WSe_2, and WTe_2): materials chemistry and applications. *Journal of Materials Chemistry A*, *5*(35): 18299–18325, 2017.

[5] Nassiri Nazif, K., Daus, A., Hong, J., Lee, N., Vaziri, S., Kumar, A., Nitta, F., Chen, M.E., Kananian, S., Islam, R., Kim, K.H. High-specific-power flexible transition metal dichalcogenide solar cells. *Nature Communications*, *12*(1): 7034, 2021.

[6] Aftab, Z., Sulania, I., Kandasami, A., Nair, L. Swift Heavy Ion-Induced Reactivity and Surface Modifications in Indium Thin Films. *ACS Omega*, *7*(36): 31869–31876, 2022.

[7] Avasthi, D. K., Mehta, G. K. *Swift heavy ions for materials engineering and nanostructuring*, Vol. 145, ISBN:9400712294, Springer Science & Business Media, 2011.

[8] Ghorbani-Asl, M., Kretschmer, S., Krasheninnikov, A. V. Two-dimensional materials under ion irradiation: from defect production to structure and property engineering. In *Defects in Two-Dimensional Materials*, pages 259–301, Elsevier, 2022.

[9] Gupta, D., Chauhan, V., Koratkar, N., Kumar, R. Electronic structure engineering of 2-D MoS_2 sputtered thin films under ion beam irradiation: Induced by controlled defect generation. *Ceramics International*, *48*(3): 2999–3019, 2022.

[10] Shi, T., Walker, R. C., Jovanovic, I., Robinson, J. A. Effects of energetic ion irradiation on WSe_2/SiC heterostructures. *Scientific Reports*, *7*(1): 4151, 2017.

[11] Elafandi, S., Christiansen, R., Azam, N., Cichon, M., Park, M., Hamilton, M. C., Mahjouri-Samani, M. Monolayer 2D quantum materials subjected to gamma irradiation in high-vacuum for nuclear and space applications. *Applied Physics Letters*, *116*(21): 213105, 2020.

[12] Stanford, M.G., Pudasaini, P.R., Belianinov, A., Cross, N., Noh, J.H., Koehler, M.R., Mandrus, D.G., Duscher, G., Rondinone, A.J., Ivanov, I.N., Ward, T.Z. Focused helium-ion beam irradiation effects on electrical transport properties of few-layer WSe_2: enabling nanoscale direct write homo-junctions. *Scientific Reports*, *6*(1): 27276, 2016.

[13] Zhang, B.Q., Chen, J.-S., Niu, H.L., Mao, C.J., Song, J.M. Synthesis of ultrathin WSe_2 nanosheets and their high-performance catalysis for conversion of amines to imines. *Nanoscale*, *10*(43): 20266–20271, 2018.

[14] Terrones, H., Corro, E.D., Feng, S., Poumirol, J.M., Rhodes, D., Smirnov, D., Pradhan, N.R., Lin, Z., Nguyen, M.A.T., Elías, A.L., Mallouk, T.E. New First Order Raman-active Modes in Few Layered Transition Metal Dichalcogenides. *Scientific Reports*, *4*(1): 4215, 2014.

[15] Bhatt, S. V, Deshpande, M. P., Sathe, V., Rao, R., Chaki, S. H. Raman spectroscopic investigations on transition-metal dichalcogenides MX_2 (M= Mo, W; X= S, Se) at high pressures and low temperature. *Journal of Raman Spectroscopy*, *45*(10): 971–979, 2014.

[16] Paul, N., Hazarika, S., Saha, A., Mohanta, D. Optical emission, vibrational feature, and shear-thinning aspect of Tb^{3+} doped Gd_2O_3 nanoparticle-based novel ferrofluids irradiated by gamma photons. *Journal of Applied Physics*, *114*(13): 134903, 2013.

[17] Shah, S. N. A., Shahabuddin, S., Sabri, M. F. M., Salleh, M. F. M., Said, S. M., Khedher, K. M. Thermal conductivity, rheology and stability analysis of 2D tungsten disulphide-doped polyaniline-based nanofluids: An experimental investigation. *International Journal of Energy Research*, *45*(2): 1550–1575, 2021.

[18] Li, M., Wu, Q., Moon, R. J., Hubbe, M. A., Bortner, M. J. Rheological aspects of cellulose nanomaterials: Governing factors and emerging applications. *Advanced Materials*, *33*(21): 2006052, 2021.

[19] Layek, R. K., Kundu, A., Nandi, A. K. High-performance nanocomposites of sodium carboxymethylcellulose and graphene oxide. *Macromolecular Materials and Engineering*, *298*(11): 1166–1175, 2013.

[20] Shetty, S. K., Ismayil, Noor, I. M. Effect of new crystalline phase on the ionic conduction properties of sodium perchlorate salt doped carboxymethyl cellulose biopolymer electrolyte films. *Journal of Polymer Research*, *28*(11): 415, 2021.

[21] Baboo, M., Kumar, S., Kumar, B., Sharma, K., Saxena, N. S. Vogel–Fulcher–Tammann approach for the determination of fragility of polyisoprene (cis & trans) blend by activation energy: effect of fillers (aluminum and polyaniline). *Polymer Bulletin*, *81*(5): 4629–4642, 2024.

[22] Edmondson, P. D., Zhang, Y., Moll, S., Namavar, F., Weber, W. J. Irradiation effects on microstructure change in nanocrystalline ceria–Phase, lattice stress, grain size and boundaries. *Acta Materialia*, *60*(15): 5408–5416, 2012.

[23] Grover, V., Shukla, R., Kumari, R., Mandal, B.P., Kulriya, P.K., Srivastava, S.K., Ghosh, S., Tyagi, A.K., Avasthi, D.K. Effect of grain size and microstructure on

radiation stability of CeO_2: an extensive study. *Physical Chemistry Chemical Physics*, *16*(48): 27065–27073, 2014.

[24] Hellborg, R. Ion Beams in Nanoscience and Technology. *Particle Acceleration and Detection,* Springer-Verlag Berlin Heidelberg, 2010.

[25] Tenne, R., Margulis, L., Genut, M., Hodes, G. Polyhedral and cylindrical structures of tungsten disulphide. *Nature*, *360*(6403): 444–446, 1992.

[26] Shahar, C., Zbaida, D., Rapoport, L., Cohen, H., Bendikov, T., Tannous, J., Dassenoy, F., Tenne, R. Surface Functionalization of WS_2 Fullerene-like Nanoparticles. *Langmuir*, *26*(6): 4409–4414, 2010.

[27] Curl, R. F., Smalley, R. E. Fullerenes. *Scientific American*, *265*(4): 54–63, 1991.

[28] Salam, A., Xie, G., Guo, D., Xu, W. Fabrication and tribological behavior of self-lubricating composite impregnated with synthesized inorganic hollow fullerene-like MoS_2. *Composites Part B: Engineering*, *207*: 108557, 2021.

[29] Marjanović, M., Danica, B., Srdja, P., Bojana, F., Zijah, B., Lidija, M., and Bekrić, D. Inorganic fullerene-like nanoparticles and nanotubes of tungsten disulfide as reinforcement of carbon-epoxy composites. *Fullerenes, Nanotubes and Carbon Nanostructures*, *29*(12): 1034–1044, 2021.

[30] Shlimak, I., Haran, A., Zion, E., Havdala, T., Kaganovskii, Y., Butenko, A.V., Wolfson, L., Richter, V., Naveh, D., Sharoni, A., Kogan, E. Raman scattering and electrical resistance of highly disordered graphene. *Physical Review B*, *91*(4): 45414, 2015.

[31] Sierra-Castillo, A., Haye, E., Acosta, S., Bittencourt, C., Colomer, J.F. Synthesis and Characterization of Highly Crystalline Vertically Aligned WSe_2 Nanosheets. *Applied Sciences*, *10*(3): 874, 2020.

[32] Kalita, P., Ghosh, S., Gutierrez, G., Rajput, P., Grover, V., Sattonnay, G., Avasthi, D. K. Grain size effect on the radiation damage tolerance of cubic zirconia against simultaneous low and high energy heavy ions: Nano triumphs bulk. *Scientific reports*, *11*(1): 10886, 2021.

[33] Sahin, H., Tongay, S., Horzum, S., Fan, W., Zhou, J., Li, J., Wu, J., Peeters, F.M. Anomalous Raman spectra and thickness-dependent electronic properties of WSe_2. *Physical Review B*, *87*(16): 165409, 2013.

[34] Late, D. J., Shirodkar, S. N., Waghmare, U. V, Dravid, V. P., Rao, C. N. R. Thermal expansion, anharmonicity and temperature-dependent Raman spectra of single-and few-layer $MoSe_2$ and WSe_2. *ChemPhysChem*, *15*(8): 1592–1598, 2014.

[35] Feng, C., Xiang, J., Liu, P., Xiang, B. The growth study of bilayer and monolayer WSe_2. *Materials Research Express*, *4*(9): 095703, 2017.

[36] Liu, H.J., Jiao, L., Xie, L., Yang, F., Chen, J.L., Ho, W.K., Gao, C.L., Jia, J.F., Cui, X.D., Xie, M.H. Molecular-beam epitaxy of monolayer and bilayer WSe_2: a scanning tunneling microscopy/spectroscopy study and deduction of exciton binding energy. *2D Materials*, *2*(3): 034004, 2015.

[37] Anbalagan, A.K., Hu, F.C., Chan, W.K., Gandhi, A.C., Gupta, S., Chaudhary, M., Chuang, K.W., Ramesh, A.K., Billo, T., Sabbah, A., Chiang, C.Y. Gamma-Ray Irradiation Induced Ultrahigh Room-Temperature Ferromagnetism in MoS_2 Sputtered Few-Layered Thin Films. *ACS Nano*, *17*(7): 6555–6564, 2023.

[38] Giannozzi, P., Andreussi, O., Brumme, T., Bunau, O., Nardelli, M.B., Calandra, M., Car, R., Cavazzoni, C., Ceresoli, D., Cococcioni, M., Colonna, N. Advanced capabilities for materials modelling with Quantum ESPRESSO. *Journal of physics: Condensed matter*, *29*(46): 465901, 2017.

[39] Giannozzi, P., Baseggio, O., Bonfà, P., Brunato, D., Car, R., Carnimeo, I., Cavazzoni, C., De Gironcoli, S., Delugas, P., Ferrari Ruffino, F., Ferretti, A. Quantum ESPRESSO toward the exascale. *The Journal of chemical physics*, *152*(15): 154105, 2020.

[40] Giannozzi, P., Baroni, S., Bonini, N., Calandra, M., Car, R., Cavazzoni, C., Ceresoli, D., Chiarotti, G.L., Cococcioni, M., Dabo, I., Dal Corso, A. QUANTUM ESPRESSO: a modular and open-source software project for quantum simulations of materials. *Journal of Physics: Condensed Matter*, *21*(39): 395502, 2009.

[41] Carnimeo, I., Affinito, F., Baroni, S., Baseggio, O., Bellentani, L., Bertossa, R., Delugas, P.D., Ruffino, F.F., Orlandini, S., Spiga, F., Giannozzi, P. Quantum ESPRESSO: one further step toward the exascale. *Journal of Chemical Theory and Computation*, *19*(20): 6992–7006, 2023.

[42] Perdew, J. P., Burke, K., Ernzerhof, M. Generalized gradient approximation made simple. *Physical Review Letters*, *77*(18): 3865, 1996.

[43] Ullah, H., Kim, H. J., Shin, Y.-H. Influences of vacancy and doping on electronic and magnetic properties of monolayer SnS. *Journal of Applied Physics*, *124*(6): 065102, 2018.

[44] Yang, D., Fan, X., Zhang, F., Hu, Y., Luo, Z. Electronic and magnetic properties of defected monolayer WSe_2 with vacancies. *Nanoscale research letters*, *14*: 1–9, 2019.

[45] Park, S., Mutz, N., Schultz, T., Blumstengel, S., Han, A., Aljarb, A., Li, L.J., List-Kratochvil, E.J., Amsalem, P., Koch, N. Direct determination of monolayer MoS_2 and WSe_2 exciton binding energies on insulating and metallic substrates. *2D Materials*, *5*(2): 025003, 2018.

[46] Hsu, W.T., Lu, L.S., Wang, D., Huang, J.K., Li, M.Y., Chang, T.R., Chou, Y.C., Juang, Z.Y., Jeng, H.T., Li, L.J., Chang, W.H. Evidence of indirect gap in monolayer WSe_2. *Nature communications*, *8*(1): 929, 2017.

[47] Li, J., Jia, L., Zheng, X., Peng, C., Fu, X. Structural and elastic properties of WSe_2: first-principles calculations. *Journal of Physics: Conference Series*, *1634*(1): 12145, 2020.

[48] Xu, X., Wang, C., Xiong, W., Liu, Y., Yang, D., Zhang, X., Xu, J. Strain regulated interlayer coupling in WSe_2/WS_2 heterobilayer. *Nanotechnology*, *33*(8): 085705, 2022.